

# Abundances of CNO elements in $z \sim 0.3 - 0.4$ LyC leaking galaxies

Y. I. Izotov<sup>1\*</sup>, D. Schaerer<sup>2,3</sup>, G. Worseck<sup>4</sup>, D. Berg<sup>5</sup>, J. Chisholm<sup>5</sup>,  
S. Ravindranath<sup>6</sup>, T. X. Thuan<sup>7</sup>

<sup>1</sup>*Bogolyubov Institute for Theoretical Physics, National Academy of Sciences of Ukraine, 14-b Metrolohichna str., Kyiv, 03143, Ukraine,  
E-mail: yizotov@bitp.kiev.ua*

<sup>2</sup>*Observatoire de Genève, Université de Genève, 51 Ch. des Maillettes, 1290, Versoix, Switzerland,  
E-mail: daniel.schaerer@unige.ch*

<sup>3</sup>*IRAP/CNRS, 14, Av. E. Belin, 31400 Toulouse, France*

<sup>4</sup>*Institut für Physik und Astronomie, Universität Potsdam, Karl-Liebknecht-Str. 24/25, D-14476 Potsdam, Germany,  
E-mail: gworseck@uni-potsdam.de*

<sup>5</sup>*Astronomy Department, University of Texas at Austin, 2515 Speedway, Stop C1400 Austin, TX 78712-1205, USA,  
E-mail: daberg@austin.utexas.edu, chisholm@austin.utexas.edu*

<sup>6</sup>*Space Telescope Science Institute, 3700 San Martin Drive, Baltimore, MD, 21218, USA,  
E-mail: swara@stsci.edu*

<sup>7</sup>*Astronomy Department, University of Virginia, P.O. Box 400325, Charlottesville, VA 22904-4325, USA,  
E-mail: txt@virginia.edu*

Accepted XXX. Received YYY; in original form ZZZ

## ABSTRACT

We present observations with the Space Telescope Imaging Spectrograph (STIS) onboard the *Hubble Space Telescope* of eleven Lyman continuum (LyC) leaking galaxies at redshifts,  $z$ , in the range 0.29–0.43, with oxygen abundances  $12 + \log(\text{O}/\text{H}) = 7.64 - 8.16$ , stellar masses  $M_{\star} \sim 10^{7.8} - 10^{9.8} M_{\odot}$  and  $\text{O}_{32} = [\text{O III}] \lambda 5007 / [\text{O II}] \lambda 3727$  of  $\sim 5 - 20$  aiming to detect the  $\text{C III}] \lambda 1908$  emission line. We combine these observations with the optical Sloan Digital Sky Survey (SDSS) spectra for the determination of carbon, nitrogen and oxygen abundances. Our sample was supplemented by thirty one galaxies from the literature, for which carbon, nitrogen and oxygen abundances can be derived from the *HST* and SDSS spectra. These additional galaxies, however, do not have LyC observations. We find that  $\log(\text{C}/\text{O})$  for the entire sample at  $12 + \log(\text{O}/\text{H}) < 8.1$  does not depend on metallicity, with a small dispersion of  $\sim 0.13$  dex around the average value of  $\sim -0.75$  dex. On the other hand, the  $\log(\text{N}/\text{O})$  in galaxies at  $z > 0.1$ , including LyC leakers, is systematically higher compared to the rest of the sample with lower metallicity. We find that  $\log(\text{C}/\text{O})$  slightly decreases with increasing  $M_{\star}$  from  $\sim -0.65$  at  $M_{\star} = 10^6 M_{\odot}$  to  $\sim -0.80$  at  $M_{\star} = 10^9 - 10^{10} M_{\odot}$ , whereas  $\log(\text{N}/\text{O})$  is considerably enhanced at  $M_{\star} > 10^8 M_{\odot}$ . The origin of these trends remains basically unknown. A possible solution would be to assume that the upper mass limit of the stellar initial mass function (IMF) in more massive galaxies is higher. This would result in a higher production of oxygen and a larger fraction of massive stars with stellar wind polluting the interstellar medium with nitrogen.

**Key words:** galaxies: abundances — galaxies: dwarf — galaxies: fundamental parameters — galaxies: ISM — galaxies: starburst

## 1 INTRODUCTION

The most abundant heavy element species, carbon, nitrogen and oxygen, play a crucial role in describing the chemical enrichment of galaxies. This is because oxygen is produced only by short-lived massive stars with  $M_{\star} > 10 M_{\odot}$ , whereas carbon and nitrogen are synthesized by both massive stars and longer-lived stars of lower

masses, resulting in variations of C/O and N/O abundance ratios with time. Since both the oxygen and carbon are primary elements, their abundance ratio variations as a function of oxygen abundance are expected to be flat. As for nitrogen, it can be produced in both primary and secondary processes, but the contribution of secondary nitrogen at low metallicities is small and no significant dependence of the N/O abundance ratio on oxygen abundance is expected. Indeed, it was found in many studies that the N/O abundance ratio at low oxygen abundances  $12 + \log(\text{O}/\text{H}) \leq 8.0$  is constant, suggesting

\* Corresponding author: yizotov@bitp.kiev.ua

that the N production is primary (e.g. [Izotov et al. 2006](#)), with however a significant scatter ( $\pm 0.5$  dex). This scatter may be due to the time-dependent nature of N/O abundance ratios and/or different star formation efficiencies setting different fundamental plateau values (e.g. [Henry, Edmunds & Köppen 2000](#); [Berg et al. 2020](#)). Furthermore, [Izotov et al. \(2006\)](#) suggested that the scatter can also be due to local nitrogen pollution by Wolf-Rayet stars. At higher metallicities, the secondary production of nitrogen becomes important and thus the N/O abundance ratio increases with increasing oxygen abundance.

As for carbon, abundances of its ions can be derived from the emission of weak recombination lines in the optical range, but this is practically possible only in bright H II regions, with high oxygen abundances  $12 + \log(\text{O}/\text{H}) \gtrsim 8.0$  (e.g. [Esteban et al. 2014](#)). At lower metallicities only collisionally-excited forbidden lines in the UV range can be used to derive the carbon abundance. However, rest-frame UV observations of the galaxies in the local Universe are only possible from space.

Several fundamental studies on the determination of the carbon abundances have been made with the *Hubble Space Telescope* (*HST*) starting from the pioneering work by [Garnett et al. \(1995\)](#), who found that C/O abundance ratio in low-metallicity dwarf star-forming galaxies (SFGs) linearly increases with oxygen abundance O/H. However, this finding has not been confirmed in later studies of low-metallicity SFGs. It is also inconsistent with the constant C/O abundance ratio in Milky Way halo stars with metallicities in the same range (e.g. [Akerman et al. 2004](#); [Fabbian et al. 2009](#)). Thus, [Izotov & Thuan \(1999\)](#) re-analysed observations of five galaxies from the [Garnett et al. \(1995\)](#) sample and added one more galaxy from [Thuan et al. \(1999\)](#), all with  $12 + \log(\text{O}/\text{H}) \leq 7.6$ , and found  $\log(\text{C}/\text{O})$  and  $\log(\text{C}/\text{N})$  to be constant, at  $-0.78 \pm 0.03$  and  $0.82 \pm 0.04$ , respectively. These constant abundance ratios imply that C and N at low metallicities have a primary origin.

All of the early *HST* observations were obtained with the Faint Object Spectrograph (FOS). Subsequent observations with the Cosmic Origins Spectrograph (COS) and Space Telescope Imaging Spectrograph (STIS) onboard *HST* considerably increased the number of galaxies with a determined C/O abundance ratio.

Using COS observations of 21 dwarf star-forming galaxies with  $z < 0.1$ , [Berg et al. \(2016, 2019\)](#) found no trend in C/O at low metallicity and a constant C/N ratio but with significant scatter over a larger range in oxygen abundance, indicating that carbon is predominantly produced by the same nucleosynthetic mechanisms as nitrogen. [Berg et al. \(2019\)](#) derived  $\log(\text{C}/\text{O}) = -0.71$  and  $\log(\text{C}/\text{N}) = 0.75$  with dispersion  $\sigma = 0.17$  and  $0.25$ , respectively. They also found a declining C/O ratio with increasing baryonic mass of the galaxy, due to increasing effective oxygen yields.

[Senchyna et al. \(2017\)](#) obtained *HST*/COS spectra of 10 nearby galaxies at  $z < 1$  with active ongoing star formation to study the variations in C III]  $\lambda 1907$ ,  $1909\text{\AA}$  equivalent widths (hereafter C III]  $\lambda 1908\text{\AA}$ ). Combining with archival local samples, they found that C III] emission lines with equivalent widths  $> 5\text{\AA}$  are observed only in galaxies with  $12 + \log(\text{O}/\text{H}) \lesssim 8.4$ . On average, their EW(C III]) values are similar to those obtained by [Berg et al. \(2016, 2019\)](#) and in high- $z$  star-forming galaxies. [Senchyna et al. \(2017\)](#) derived the C/O abundance ratios in their galaxies, but no analysis of these values and a comparison with other studies have been done.

[Ravindranath et al. \(2020\)](#) analyzed the *HST*/STIS near-UV (NUV) spectra for a sample of 10 “green pea” (GP) galaxies at higher redshifts,  $0.1 \leq z \leq 0.3$ . They found that the C III] EWs of GPs are in the range  $2 - 10\text{\AA}$ , overlapping with the range of values seen in low- $z$  and  $z > 2$  SFGs, but not reaching the high EW(C III])

values ( $> 15\text{\AA}$ ) seen in some  $z > 2$  SFGs (e.g. [Llerena et al. 2022](#)) and in many SFGs by [Berg et al. \(2016, 2019\)](#). [Ravindranath et al. \(2020\)](#) also determined the C/O abundance ratios in their galaxies but did not analyze or compare their values to other data sets.

In all low- $z$  studies of the carbon abundance considered above, the redshifts of the galaxies are too low for *HST* to observe the restframe wavelength range of the Lyman Continuum (LyC). On the other hand, it is important to study the CNO abundances in the LyC leaking galaxies at higher redshift to find common properties and possible differences associated with the LyC leakage with non-leaking galaxies and the lower-redshift galaxies, for which observations of the LyC are not possible. The first study of the carbon abundance in a LyC leaker was done for J1154+2443 with a very high escape fraction  $f_{\text{esc}}(\text{LyC}) = 46$  per cent, by [Schaerer et al. \(2018\)](#), who obtained  $\log(\text{C}/\text{O}) = -0.84 \pm 0.06$  from the C III]  $\lambda 1908$  and [O III]  $\lambda 4959, 5007$  line ratio. To increase the statistics of LyC leaking galaxies with a derived carbon abundance, we consider in this paper *HST*/STIS observations of a sample of 10 LyC leakers from [Izotov et al. \(2016a,b, 2018a,b\)](#) with  $f_{\text{esc}}(\text{LyC})$  in the range 2–72 per cent and very compact morphology. A main goal of these observations was to study how high-ionization emission lines He II  $\lambda 1640$  and C IV  $\lambda 1549, 1551$  are linked to LyC leakage, as done by [Schaerer et al. \(2022\)](#). But they allow also to derive carbon abundances in galaxies with higher stellar masses, compared to that of low- $z$  galaxies studied by [Berg et al. \(2016, 2019\)](#), and in a wide range of the LyC escape fraction. That is the aim of the present study. All these galaxies were initially selected from the Sloan Digital Sky Survey (SDSS). Their coordinates, redshifts,  $\text{O}_{32} = [\text{O III}] \lambda 5007 / [\text{O II}] \lambda 3727$  flux ratios, stellar masses, and oxygen abundances are given in Table 1. We also included the galaxy J1154+2443 from the [Izotov et al. \(2016a,b, 2018a,b\)](#) sample, which was observed in program GO 15433 (PI: D. Schaerer) with the same STIS setup and reduced in a similar manner ([Schaerer et al. 2018](#)). However, [Schaerer et al. \(2018\)](#) derived a C/O abundance ratio from only a four-orbits exposure, whereas we use the final spectrum of J1154+2443 with twice the exposure time.

The *HST*/STIS observations of the LyC leaking galaxies are discussed in Section 2. The method for the determination of element abundances is described in Section 3. In Section 4 we discuss the derived CNO abundances and compare them with the results of previous studies. We summarize our findings in Section 5.

## 2 *HST*/STIS OBSERVATIONS AND DATA REDUCTION

*HST*/STIS spectroscopy of the 10 LyC leakers was obtained in program GO 15941 (PI: D. Schaerer) during the period June 2020 – June 2022 ([Schaerer et al. 2022](#)). The observational details are presented in Table 2. We also included in the Table the galaxy J1154+2443, for which some results of STIS spectroscopy were published in [Schaerer et al. \(2018\)](#).

The galaxies were directly acquired by STIS/CCD optical imaging using an image obtained with the long-pass filter F28X50LP. The spectra were obtained with the STIS/NUV-MAMA low-resolution grating G230L, the central wavelength  $2376\text{\AA}$ , and the  $52 \text{ arcsec} \times 0.5 \text{ arcsec}$  slit, resulting in a spectral resolution  $R = 750$  and wavelength coverage of  $1570 - 3180\text{\AA}$ . This setup allows to gather almost all light from our compact galaxies ([Izotov et al. 2016a,b, 2018a,b](#)), which have small angular sizes,  $\sim 1$  arcsec in diameter, according to SDSS photometry. The individual sub-exposures have somewhat different (by less than  $1\text{\AA}$ ) spectral ranges and they were reduced to a common wavelength range, which

**Table 1.** Coordinates and characteristics derived from the COS and SDSS spectra

Name	R.A.(2000.0)	Dec.(2000.0)	$z^a$	$O_{32}^b$	$\log(M_*/M_\odot)^c$	$12+\log(O/H)^d$	$\log(N/O)$	$f_{\text{esc}}(\text{LyC})$
J0901+2119	09:01:45.61	+21:19:27.70	0.29932	20.0	9.80	$8.16\pm 0.02$	$-1.22\pm 0.07$	$0.027\pm 0.007$
J0925+1403	09:25:32.37	+14:03:13.06	0.30121	5.9	8.91	$7.91\pm 0.01$	$-1.12\pm 0.04$	$0.078\pm 0.008$
J1011+1947	10:11:38.28	+19:47:20.90	0.33219	19.2	9.00	$7.99\pm 0.01$	$-0.85\pm 0.09$	$0.114\pm 0.018$
J1152+3400	11:52:04.88	+34:00:49.88	0.34197	3.9	9.59	$8.00\pm 0.02$	$-1.17\pm 0.10$	$0.132\pm 0.011$
J1154+2443	11:54:48.85	+24:43:33.02	0.36900	11.5	8.20	$7.65\pm 0.02$	$-1.30\pm 0.25$	$0.460\pm 0.020$
J1243+4646	12:43:00.63	+46:46:50.40	0.43166	11.2	7.80	$7.89\pm 0.01$	$-1.14\pm 0.16$	$0.726\pm 0.097$
J1248+4259	12:48:10.48	+42:59:53.60	0.36300	19.7	8.20	$7.64\pm 0.01$	$-1.07\pm 0.12$	$0.022\pm 0.007$
J1256+4509	12:56:44.15	+45:09:17.00	0.35311	16.3	8.80	$7.87\pm 0.01$	$-1.01\pm 0.12$	$0.380\pm 0.057$
J1333+6246	13:33:03.96	+62:46:03.78	0.31816	4.8	8.50	$7.76\pm 0.02$	$-1.54\pm 0.19$	$0.056\pm 0.015$
J1442-0209	14:42:31.39	-02:09:52.03	0.29364	7.9	8.96	$7.93\pm 0.01$	$-1.25\pm 0.09$	$0.074\pm 0.010$
J1503+3644	15:03:42.83	+36:44:50.75	0.35562	4.9	8.22	$7.95\pm 0.01$	$-1.25\pm 0.09$	$0.058\pm 0.006$

<sup>a</sup> $z$  is the redshift.

<sup>b</sup> $O_{32}$  is the extinction-corrected ratio  $I([\text{O III}]\lambda 5007)/I([\text{O III}]\lambda 3272)$ .

<sup>c</sup> $M_*$  is the stellar mass.

<sup>d</sup>Oxygen abundance derived by the direct  $T_e$  method.

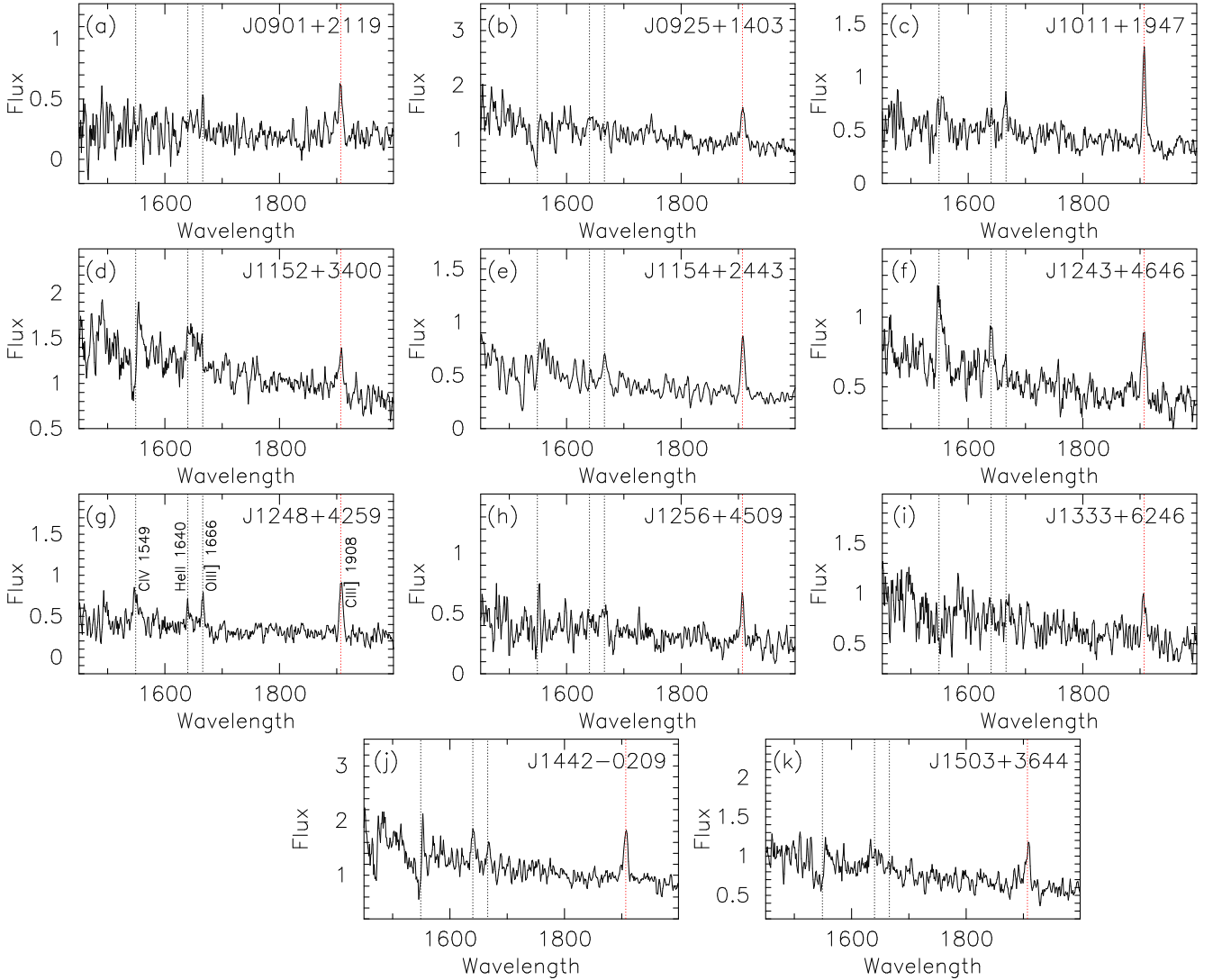


**Figure 1.** *HST/STIS* spectra of LyC leaking galaxies with the G230L grating. The spectra are shifted to rest-frame wavelengths. The strongest lines are labelled in (g) and their locations are marked by vertical red dotted lines (C III]  $\lambda 1908$ ) and by vertical black dotted lines (other lines). Fluxes and wavelengths are expressed in  $10^{-16} \text{ erg s}^{-1} \text{ cm}^{-2} \text{ \AA}^{-1}$  and  $\text{\AA}$ , respectively.

**Table 2.** *HST*/STIS observations

Name	Date	Exposure time (s)	
		Acquisition	Science
J0901+2119	2021-04-13	440	12539
J0925+1403	2021-03-21	200	7387
J1011+1947	2021-04-17	340	12734
J1152+3400	2021-02-04	140	7600
J1154+2443	2018-04-28	360	10418
	2019-01-02	360	9290
J1243+4646	2021-01-30	420	13219
J1248+4259	2021-02-03	300	10339
J1256+4509	2022-05-25	580	7012
	2022-06-28	290	4376
J1333+6246	2021-12-22	180	11271
J1442-0209	2020-06-18	180	7406
J1503+3644	2022-02-05	180	7500

is the same for all exposures, co-added using the `IRAF dispacor` routine, and the one-dimensional (1D) spectrum was extracted using `IRAF's apall` routine.

The rest-frame UV spectra of all galaxies are shown in Fig. 1. The locations of the four brightest lines in all panels are identified by vertical black (highlighting the C IV  $\lambda$ 1550, He II  $\lambda$ 1640, and O III]  $\lambda$ 1666Å) and red dotted lines (highlighting the C III] lines) and are labelled in (g). The lines in some spectra are weak and barely detected or non-detected. The only line which is clearly detected in all spectra, is the C III]  $\lambda$ 1908Å emission line, which, in fact, is a blended doublet. This allows us to derive carbon abundance in all studied galaxies using *HST* UV and SDSS optical spectra.

The O III]  $\lambda$ 1666Å and C III]  $\lambda$ 1908Å emission line fluxes,  $F(\text{O III] } \lambda 1666\text{Å})$  and  $F(\text{C III] } \lambda 1908\text{Å})$ , and rest-frame equivalent widths  $\text{EW}(\text{O III] } \lambda 1666\text{Å})$  and  $\text{EW}(\text{C III] } \lambda 1908\text{Å})$  have been measured using the `IRAF splot` routine. The flux errors were obtained using eq. 1 by Berg et al. (2019). The results of measurements are shown in Table 3 together with the observed fluxes  $F(\text{H}\beta)$  and rest-frame equivalent widths  $\text{EW}(\text{H}\beta)$  of the  $\text{H}\beta$  emission line, which are taken from Izotov et al. (2016a,b, 2018a,b). We note that the equivalent widths  $\text{EW}(\text{C III] } \lambda 1908\text{Å})$  of  $z \sim 0.3 - 0.4$  LyC leakers are high. They are similar to those in the lower-redshift galaxies studied by Berg et al. (2016, 2019).

In addition to the sample of LyC leakers, we construct a comparison sample of lower-redshift compact dwarf galaxies with strong emission lines observed with COS and studied by Berg et al. (2016, 2019) and observed with STIS and studied by Ravindranath et al. (2020), totalling 31 galaxies. We extracted *HST* and SDSS spectra from the respective data bases and measured emission line fluxes and equivalent widths, similarly to measurements for the LyC leaker sample. Results of the measurements are given in Tables B1 – B3.

### 3 THE METHOD

We derive CNO element abundances in both the LyC leakage sample and the comparison sample using the STIS-MAMA (this paper, Ravindranath et al. 2020), COS (Berg et al. 2016, 2019) and SDSS spectra, corrected for both the Milky Way and internal extinction. The galaxy internal interstellar extinction has been obtained from the observed decrement of hydrogen emission lines in the SDSS spectra (Izotov, Thuan & Lipovetsky 1994) after correcting them for the Milky Way extinction with  $A(V)_{\text{MW}}$  from the NED and adopting the Cardelli, Clayton & Mathis (1989) reddening law with

$R(V)_{\text{MW}} = 3.1$ . Second, the fluxes of emission lines at the rest-frame wavelengths were corrected for the internal extinction of galaxies adopting the Cardelli et al. (1989) reddening law with  $R(V)_{\text{int}} = 2.7$  and the extinction coefficient  $C_{\text{int}}(\text{H}\beta)$  derived from the Balmer decrement, including all observed hydrogen lines of the Balmer series, after correcting for the Milky Way extinction.

The extinction coefficient is determined by minimizing the deviations from the theoretical case B ratios of all extinction-corrected hydrogen flux ratios. We have checked with the `CLOUDY` photoionized H II models with zero extinction and various column number densities of the uniform H I envelopes surrounding the H II region, that the modelled hydrogen flux ratios are nearly unchanged in models with  $N(\text{H I})$  greater than  $10^{17} \text{ cm}^{-2}$ , corresponding to an optical depth of  $\sim 1$  in the Lyman continuum, and they are consistent with the case B ratios. Deviations from the case B ratios are seen only at lower  $N(\text{H I})$ . In particular, the  $\text{H}\alpha/\text{H}\beta$  and  $\text{H}\gamma/\text{H}\beta$  flux ratios in models with these low column number densities are respectively lower and higher than the case B ratios. Thus, our correction for extinction is valid for high H I column densities where the LyC escape fraction is low.

We select  $R(V)_{\text{int}} = 2.7$  because the observed FUV spectra of LyC leaking galaxies are better fit by extrapolating the SDSS optical spectra compared to that with a reddening law by Cardelli et al. (1989) with a more common  $R(V)_{\text{int}} = 3.1$  (Izotov et al. 2016b, 2018b).

However, the reddening law by Cardelli et al. (1989) has a NUV dust bump, whereas it is not seen in galaxies studied in this paper. This bump does not affect the intensities of the O III]  $\lambda$ 1666 emission line, but may slightly change the intensities of the C III]  $\lambda$ 1908 emission line in some galaxies from the LyC leaking sample and some GP galaxies from Ravindranath et al. (2020). Therefore, we excluded this feature replacing values of the reddening law in this range with the values interpolated from the values outside the bump. Then the extinction-corrected flux  $I$  is derived from the observed flux  $F$  using the relation  $I = F \times 10^{C(\lambda)}$ . The extinction coefficients  $C_{\text{int}}(\text{H}\beta)$ ,  $C_{\text{int}}(\text{O III] } \lambda 1666)$  and  $C_{\text{int}}(\text{C III] } \lambda 1908)$  for the  $\text{H}\beta$ , O III]  $\lambda$ 1666 and C III]  $\lambda$ 1908 emission lines for the LyC leakage sample are presented in Table 3 and for the comparison sample in Tables B1 – B3.

Finally, the extinction-corrected emission lines in the optical range measured in the SDSS spectra are used to derive oxygen and nitrogen ionic and total abundances following the methods described in Izotov et al. (2006). As for  $\text{C}^{2+}$  abundance, we use the relation by Izotov & Thuan (1999)

$$\frac{\text{C}^{2+}}{\text{O}^{2+}} = 0.093 \exp\left(\frac{4.656}{t}\right) \frac{I(\text{C III] } \lambda 1908)}{I([\text{O III] } \lambda 4959 + \lambda 5007)} \quad (1)$$

to derive the  $\text{C}^{2+}/\text{O}^{2+}$  abundance ratio, where  $t = T_e/10^4\text{K}$ . We also use the O III]  $\lambda$ 1666Å emission line for the determination of the  $\text{C}^{2+}/\text{O}^{2+}$  abundance ratio using

$$\frac{\text{C}^{2+}}{\text{O}^{2+}} = 0.15 \exp\left(\frac{1.1054}{t}\right) \frac{I(\text{C III] } \lambda 1908)}{I([\text{O III] } \lambda 1666)} \quad (2)$$

(Erb et al. 2010). However, the O III]  $\lambda$ 1666Å emission line in spectra shown in Fig. 1 and in galaxies from Ravindranath et al. (2020) is weak or nondetected. Therefore, in the analysis of element abundances we mainly use the C/O abundance ratios obtained using strong optical [O III] emission lines. On the other hand, the C/O ratios derived from the C III] and UV O III] emission lines are used to check the consistency of the abundances derived by two methods.

The ratio of total C and O abundances can be derived from the



**Table 3.** Characteristics for the determination of the C/O abundance ratio in LyC leaking galaxies

Name	$F^a$ (C III) $\lambda 1908$	EW <sup>b</sup> (C III) $\lambda 1908$	$F^a$ (O III) $\lambda 1666$	EW <sup>b</sup> (O III) $\lambda 1666$	$F^a$ (H $\beta$ ) $\lambda 4861$	EW <sup>b</sup> (H $\beta$ ) $\lambda 4861$	$C_{\text{int}}^c$ (H $\beta$ ) $\lambda 4861$	$C_{\text{int}}^c$ (C III) $\lambda 1908$	$C_{\text{int}}^c$ (O III) $\lambda 1666$	corr. <sup>d</sup>
J0901+2119	4.5±1.3	16.7±5.0	1.4±1.2	4.2±3.6	16.8±0.9	255±16	0.22±0.04	0.53±0.10	0.55±0.10	1.333
J0925+1403	7.4±1.4	6.4±1.2	...	...	28.8±1.1	177±12	0.21±0.06	0.51±0.15	0.53±0.15	1.000
J1011+1947	6.5±0.7	18.2±2.0	3.7±1.3	6.7±2.4	13.9±0.8	237±30	0.17±0.04	0.41±0.10	0.42±0.10	1.111
J1152+3400	7.7±1.2	4.8±0.8	...	...	23.3±0.7	198±10	0.10±0.06	0.24±0.14	0.25±0.15	1.111
J1154+2443	5.7±0.7	12.4±1.5	4.0±1.8	7.3±3.3	7.7±0.4	220±14	0.07±0.05	0.17±0.12	0.17±0.12	1.111
J1243+4646	6.6±1.0	10.9±1.7	1.6±0.9	2.0±1.2	11.4±0.4	221±10	0.09±0.04	0.22±0.10	0.22±0.10	1.000
J1248+4259	6.8±0.9	19.0±2.5	3.1±1.1	6.9±2.4	21.8±0.6	426±12	0.22±0.04	0.52±0.09	0.54±0.10	1.176
J1256+4509	4.3±0.9	14.3±3.2	...	...	9.2±0.4	253±17	0.10±0.05	0.23±0.11	0.23±0.12	1.429
J1333+6246	4.9±1.5	7.0±2.2	...	...	9.3±0.3	194±13	0.07±0.09	0.17±0.22	0.17±0.22	1.282
J1442-0209	9.5±1.5	8.2±1.3	4.5±1.7	3.3±1.2	29.9±2.1	312±12	0.14±0.06	0.37±0.16	0.38±0.16	1.111
J1503+3644	6.4±1.3	8.3±1.6	...	...	19.4±0.6	297±12	0.13±0.07	0.31±0.17	0.32±0.17	1.250

Name	$t(\text{O III})^e$	$I(\lambda)/I(\text{H}\beta)^f$ (C III) $\lambda 1908$	$I(\lambda)/I(\text{H}\beta)^f$ (O III) $\lambda 1666$	$I(\lambda)/I(\text{H}\beta)^f$ ([O II]) $\lambda 3727$	$I(\lambda)/I(\text{H}\beta)^f$ ([O III]) $\lambda 5007$	$\log(\text{C/O})_{\text{opt}}^g$	$\log(\text{C/O})_{\text{UV}}^h$
J0901+2119	1.22±0.08	0.70±0.21	0.22±0.19	0.82±0.04	6.55±0.26	-0.456±0.291	-0.702±0.410
J0925+1403	1.50±0.09	0.49±0.09	...	1.26±0.05	6.08±0.20	-0.925±0.183	...
J1011+1947	1.46±0.08	0.69±0.07	0.40±0.14	0.30±0.02	8.07±0.19	-0.731±0.111	-0.809±0.157
J1152+3400	1.34±0.09	0.49±0.08	...	1.06±0.06	5.71±0.26	-0.734±0.215	...
J1154+2443	1.83±0.14	1.01±0.12	0.72±0.32	0.43±0.03	5.78±0.16	-0.768±0.124	-0.900±0.175
J1243+4646	1.57±0.14	0.79±0.12	0.18±0.10	0.54±0.05	7.26±0.20	-0.780±0.256	-0.446±0.361
J1248+4259	1.88±0.12	0.70±0.15	0.36±0.13	0.49±0.03	5.84±0.14	-0.963±0.121	-0.751±0.171
J1256+4509	1.61±0.14	0.92±0.19	...	0.44±0.04	7.23±0.21	-0.725±0.215	...
J1333+6246	1.78±0.22	0.75±0.23	...	1.30±0.11	6.23±0.41	-0.959±0.281	...
J1442-0209	1.46±0.08	0.64±0.10	0.31±0.12	0.94±0.05	6.24±0.26	-0.760±0.165	-0.841±0.233
J1503+3644	1.49±0.10	0.61±0.12	...	1.34±0.08	6.54±0.32	-0.849±0.198	...

<sup>a</sup>Observed flux in  $10^{-16}$  erg s<sup>-1</sup> cm<sup>-2</sup>.

<sup>b</sup>Restframe equivalent width in Å.

<sup>c</sup>Extinction coefficient for H $\beta$ , C III  $\lambda 1908$  and O III  $\lambda 1666$  emission lines.

<sup>d</sup>Correction factor used to adjust observed UV spectrum with the modelled SED.

<sup>e</sup> $t(\text{O III}) = T_e(\text{O III})/10^4\text{K}$ , where  $T_e(\text{O III})$  is the electron temperature in O<sup>2+</sup> zone derived by the direct method.

<sup>f</sup>Extinction-corrected flux ratios.

<sup>g</sup>C/O abundance ratio is derived using C III  $\lambda 1908$  and [O III]  $\lambda 4959, 5007$  emission-line fluxes.

<sup>h</sup>C/O abundance ratio is derived using C III  $\lambda 1908$  and O III  $\lambda 1666$  emission-line fluxes.

relation

$$\frac{C}{O} = ICF \left( \frac{C}{O} \right) \frac{C^{2+}}{O^{2+}}, \quad (3)$$

where the ionization correction factor  $ICF$  is determined as a ratio of O<sup>2+</sup> and C<sup>2+</sup> volume number fractions  $x(\text{O}^{2+})$  and  $x(\text{C}^{2+})$  in the H II region:

$$ICF \left( \frac{C}{O} \right) = \frac{x(\text{O}^{2+})}{x(\text{C}^{2+})}. \quad (4)$$

To derive  $ICF(\text{C/O})$  we use the observable  $\text{O}_{32} = [\text{O III}] \lambda 5007 / [\text{O II}] \lambda 3727$ , which is the characteristic of the H II region ionization state and depends on the ionization parameter. The  $\text{O}_{32}$  ratio can directly be derived from the extinction-corrected SDSS optical spectrum.

We use the CLOUDY v17.01 code (Ferland et al. 2013) to calculate a series of spherical uniform H II region models, varying in wide ranges of different parameters such as metallicity, production rate of the ionizing radiation  $Q$ , number density, filling factor, etc. In our calculations we assume that the escape fraction of ionizing radiation is zero, i.e. models are ionization-bounded. Therefore, the modelled  $\text{O}_{32}$  is not affected by the LyC leakage. Fortunately, LyC escape fractions in most galaxies from our sample are low,  $\lesssim 10$  per

cent. Furthermore, C III and [O III] emission lines are formed in the inner parts of the H II region, at variance with the [O II] emission, implying that the effect of the leakage on the ionization correction factor is likely small. The results of our calculations are shown in Fig. 2a by black dots. These data can be fitted by the relation

$$ICF \left( \frac{C}{O} \right) = 0.12295y^3 - 0.22010y^2 + 0.49088y + 0.67775 \quad (5)$$

(red line), where  $y = \log(\text{O}_{32})$ . For comparison, the relations between  $ICF(\text{C/O})$  and  $\text{O}_{32}$  obtained by Berg et al. (2019) for the metallicities  $Z = 0.1 Z_{\odot}$  and  $0.2 Z_{\odot}$  are shown by blue lines. All relations are in very good agreement for  $\text{O}_{32} \lesssim 10$ , but differ somewhat (by  $\lesssim 10$  per cent in  $ICF(\text{C/O})$  at fixed  $\text{O}_{32}$ ) for  $\text{O}_{32} > 10$ . It is seen in Fig. 2a that the ionization correction factor, and thus the C/O abundance ratio, can be somewhat overestimated because the  $\text{O}_{32}$  ratio in these galaxies may increase due to LyC leakage.

To study the possible impact of LyC leakage on  $ICF$ , we consider a set of models with varying column densities  $N(\text{H I})$  of neutral hydrogen in the uniform neutral gas envelope surrounding the H II region. Models with high and low  $N(\text{H I})$  correspond to ionization-bounded and density-bounded H II regions, respectively. In Fig. 2b are shown, by black and magenta dots, models with  $N(\text{H I})$

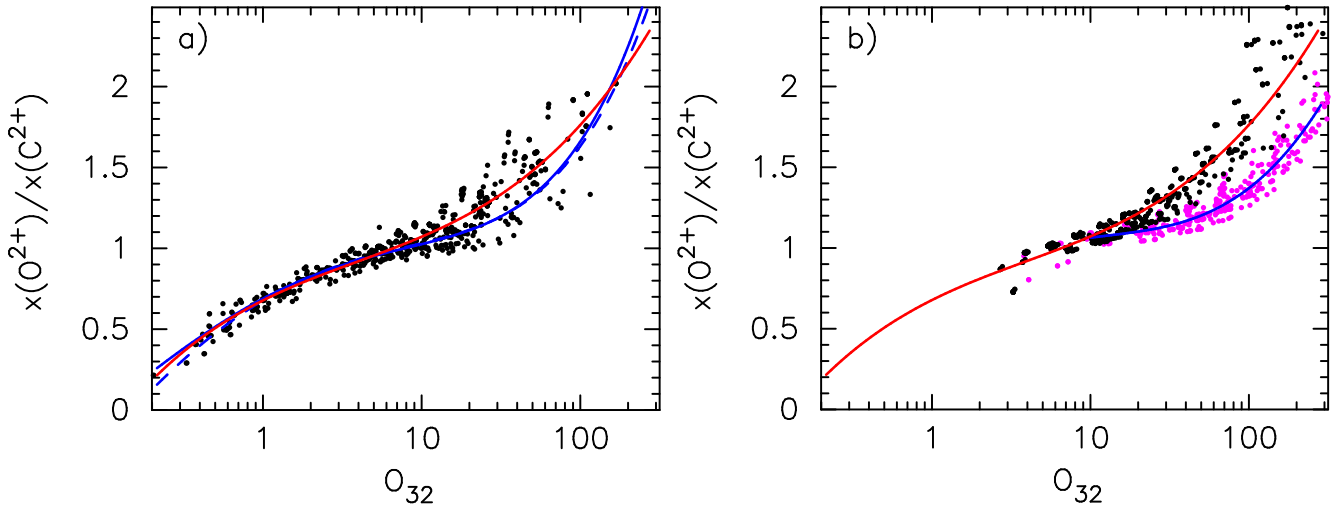


**Figure 2.** **a)** The dependence of the ionization correction factors  $ICF(C/O) = x(O^{2+})/x(C^{2+})$  on the  $O_{32} = [O\ III] \lambda 5007/[O\ II] \lambda 3727$  emission-line ratios calculated for spherical uniform ionization-bounded H II regions with the CLOUDY v. 17.01 code (Ferland et al. 2013). Here  $x(O^{2+})$  and  $x(C^{2+})$  are volume number fractions of the respective ions. The red line is the fit to the models (Eq. 5). For comparison, by the blue solid and blue dashed lines, are shown the relations for  $Z = 0.1 Z_{\odot}$  and  $0.2 Z_{\odot}$  from Berg et al. (2019), respectively. **b)** The dependence of the ionization correction factors  $ICF(C/O)$  on the  $O_{32}$  ratio for uniform H II regions with a starburst age of 2 Myr, surrounded by an envelope of neutral gas with various column number densities  $N(H\ I)$ . The models with  $N(H\ I) \geq 10^{18.5} \text{ cm}^{-2}$  are represented by black dots, whereas magenta dots are models with  $N(H\ I) \leq 10^{18.0} \text{ cm}^{-2}$ , which are fitted by the blue line. The red line is the same as in **a)**.

$\geq 10^{18.5} \text{ cm}^{-2}$  and  $\leq 10^{18.0} \text{ cm}^{-2}$ , respectively. It is seen that the models with high  $N(H\ I)$  follow the relation Eq. 5 for ionization-bounded H II regions (red line), whereas models with low  $N(H\ I)$  are offset to higher  $O_{32}$  and their distribution can be fit by the relation

$$ICF\left(\frac{C}{O}\right) = 0.26863y^3 - 0.89647y^2 + 1.11594y + 0.57551. \quad (6)$$

This offset is presumably caused by the reduced intensity of  $[O\ II] \lambda 3727$  emission line and thus by the high  $O_{32}$  ratio in the density-bounded H II regions. Therefore, the use of the relation Eq. 5 for galaxies with high LyC leakage would result in a somewhat overestimated C/O abundance ratio, by  $\lesssim 15$  per cent, adopting the observed range of  $O_{32} \lesssim 15 - 20$ . However, the LyC escape fraction is high ( $> 30$  per cent) in only three out of eleven galaxies in our sample. Furthermore, the LyC escape fraction in the galaxies from the comparison sample is not known. Therefore, for lack of more information, we adopt the relation Eq. 5 to determine the  $ICF$  for all our galaxies.

The C/O abundance ratios of LyC leaking galaxies and galaxies from the comparison sample derived by the two methods using UV and optical oxygen emission lines, respectively, are shown in Table 3 and Tables B1 – B3, respectively. The ratios derived by the method using optical  $[O\ III]$  emission lines can be subject to differences in spectroscopic apertures used in the UV and optical ranges. However, many of the selected galaxies are very compact, therefore the effect of different apertures is likely small. The spectra can also be subject to uncertainties in data reduction and absolute flux calibration. Specifically, for spectrographs using MAMA detectors in the UV (both the STIS and COS) some data can be lost if the buffer time for saving the data is non optimally selected. We assume that the derived C/O abundance ratios are reliable if the observed STIS (or COS) spectrum is consistent with the extrapolation of the attenuated SED, which is modelled from the SDSS spectrum. This requirement implies that emission in both the UV and optical ranges is dominated only by radiation of the same massive stars. This is likely the case, because equivalent widths  $EW(H\beta)$  in spectra of all

galaxies considered here are high,  $> 100\text{\AA}$  (Table 3, Tables B1 – B3).

We use the SDSS spectra of our LyC leakers and galaxies from a comparison sample to fit the SEDs. These SEDs are also used to derive the stellar masses. Briefly, the fitting method, using a two-component model (young instantaneous burst with an age  $< 10$  Myr and an older continuous star formation at ages  $> 10$  Myr), is described in Izotov et al. (2018a,b). The model includes a nebular continuum emission. Its contribution is determined by the ratio of the observed  $H\beta$  equivalent width  $EW(H\beta)$  to the value of  $\sim 900 - 1100\text{\AA}$  expected for the pure nebular recombination emission for the range of the electron temperature  $T_e = 10000 - 20000\text{K}$  (e.g. Aller 1984). A  $\chi^2$  minimisation technique was used to fit the continuum in the rest-frame wavelength range  $\sim 3000 - 6500\text{\AA}$  and to reproduce the observed  $H\beta$  and  $H\alpha$  equivalent widths. Inclusion of  $EW(H\beta)$  and  $EW(H\alpha)$  in minimisation is critically important because they constrain the age of the starburst and flux of the ionizing radiation shortward  $912\text{\AA}$  and thus the modelled continuum in the UV range at longer wavelengths.

In Fig. 3 we present the modelled stellar SEDs for the LyC leakers attenuated with an extinction coefficients  $C(H\beta)$  derived from the Balmer decrement (Table 3) and Cardelli et al. (1989) reddening laws with two values of  $R(V) = 2.7$  (black lines) and  $3.1$  (red lines). They, together with the fluxes derived from the GALEX FUV and NUV magnitudes and SDSS  $u, g, r, i, z$  magnitudes (magenta filled circles), are superposed upon both the rest-frame COS (light-grey line in the UV range, Izotov et al. 2016a,b, 2018a,b), STIS (dark-grey line, this paper) and SDSS (light-grey line in the optical range) spectra. For all galaxies we find that the modelled SEDs follow the continua of the COS/FUV and STIS/NUV spectra fairly well, implying that there is no considerable effect of different apertures or offsets which may be caused by the improper buffer time and absolute flux calibration. The photometric and spectroscopic data are also in fair agreement. This gives us confidence that the UV fluxes of our LyC leaking galaxies are robust and are not affected much by

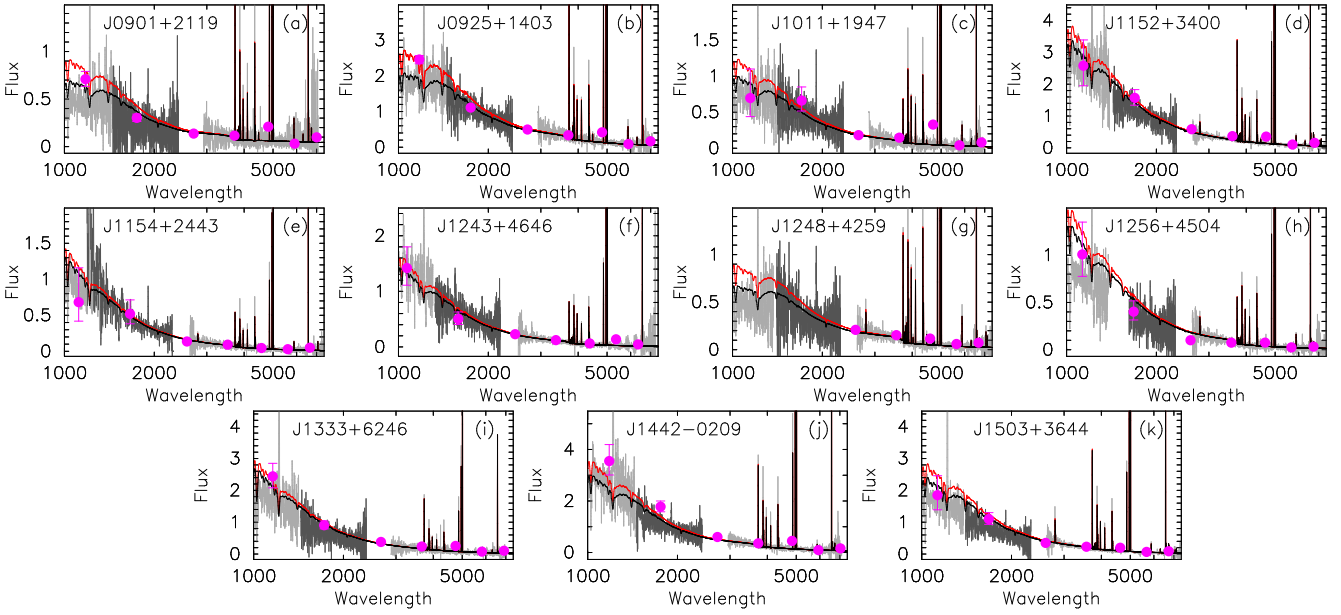


**Figure 3.** The comparison of the observed *HST*/COS (light-grey lines in the UV range) (Izotov et al. 2016a,b, 2018a,b), *HST*/STIS (dark grey lines) and SDSS (light-grey lines in the optical range) spectra with the SEDs in the optical range and their extrapolations to the UV range. The extrapolations are attenuated adopting the Cardelli, Clayton & Mathis (1989) reddening law, the derived  $C(H\beta)$  and two  $R(V)$  values of 2.7 (black line) and 3.1 (red line). For comparison, the photometric fluxes obtained from the *GALEX* FUV, NUV and SDSS  $u, b, r, i, z$  magnitudes are shown by filled magenta circles. All data are reduced to the rest-frame wavelength scale.

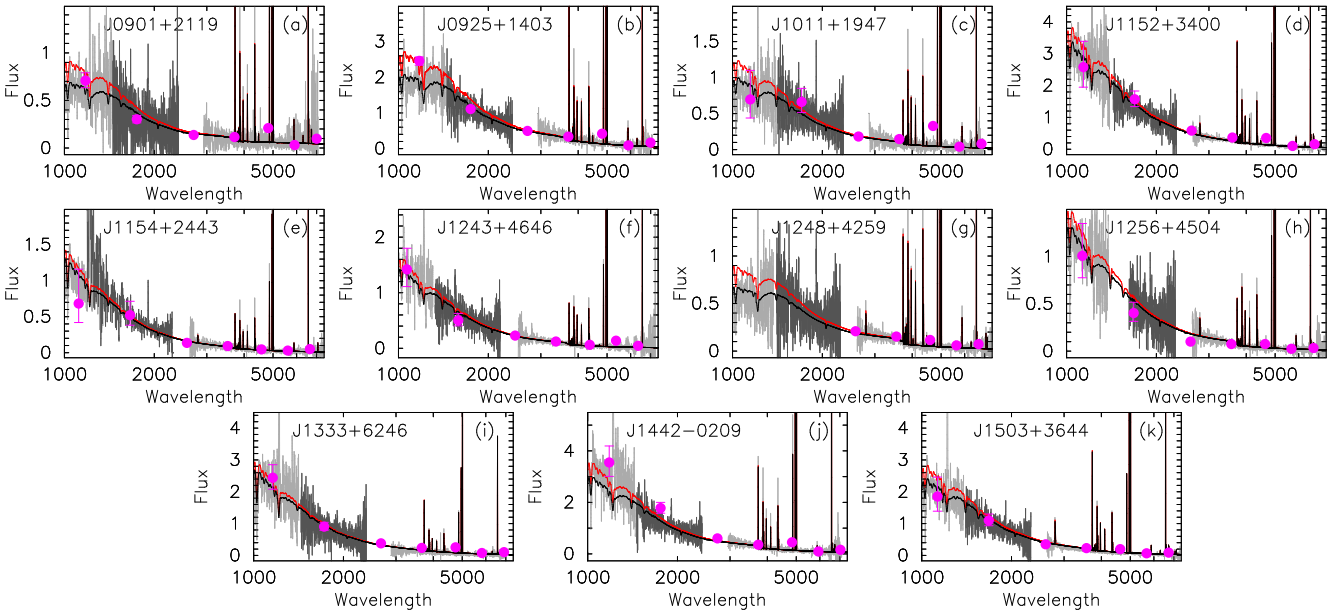


**Figure 4.** The same as in Fig. 3 but with the UV spectra scaled to the SEDs with  $R(V) = 2.7$  (black line) at  $\lambda = 1908\text{\AA}$ .

the effects discussed above. But still some small offsets between the observed UV spectra and SEDs are present for some galaxies. These offsets are considerably higher in the FUV range, than in the NUV range. Therefore, we introduce scaling factors (“corr” in Table 3) to adjust the observed UV spectra to the attenuated SEDs at the rest-frame wavelength  $1908\text{\AA}$ . For this we adopted the attenuated SEDs with  $R(V) = 2.7$  (black lines) which better fit the COS FUV and NUV observed spectra compared to other attenuated SEDs in Fig. 3, and multiply observed UV spectra by these scaling factors. The adjusted spectra are represented in Fig. 4 and they show good coincidence with the attenuated SEDs (black lines).

The spectra of galaxies from the comparison sample were similarly adjusted with the SEDs (Figs. A1 - A6) using scaling factors given in Tables B1 – B3.

We note, however, that the stellar mass derived from our SEDs may be somewhat underestimated because the infrared range is not included in the fitting. Unfortunately, both the galaxies from our and the comparison sample are faint, and none of them is included in the 2MASS catalogue. However, some of the brighter galaxies are present in the AllWISE catalogue, at the longer wavelengths of 3.4, 4.6, 12, 22  $\mu\text{m}$ . It has been shown, e.g. in Izotov et al. (2014), that for most compact star-forming galaxies the 3.4  $\mu\text{m}$  – 4.6  $\mu\text{m}$  colour in

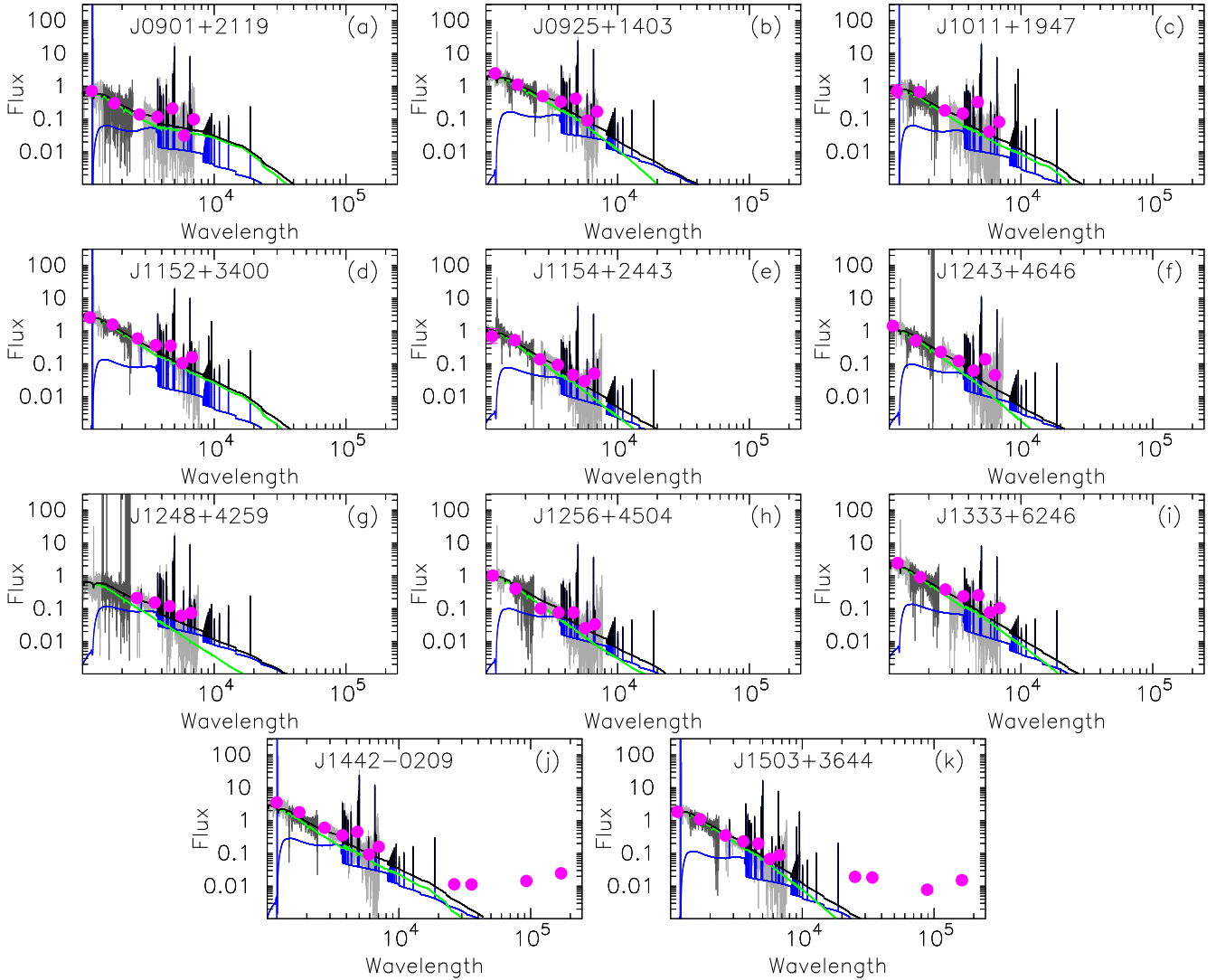


**Figure 5.** The comparison of the observed *HST*/COS (light-grey lines in the UV range) (Izotov et al. 2016a,b, 2018a,b), *HST*/STIS (dark grey lines) and SDSS (light-grey lines in the optical range) spectra with the SEDs in the optical range and their extrapolations to the UV and infrared ranges. Stellar and nebular SEDs are shown by green and blue lines, respectively, and the total (stellar+nebulars) SEDs are represented by black lines. The photometric fluxes obtained from the *GALEX* FUV, NUV, SDSS *u, b, r, i, z* and *WISE* W1 ( $3.4 \mu\text{m}$ ), W2 ( $4.6 \mu\text{m}$ ), W3 ( $12 \mu\text{m}$ ), W4 ( $22 \mu\text{m}$ ) mid-infrared magnitudes are shown by filled magenta circles.

the range 0 – 0.5 mag corresponds to stellar and nebular emission, whereas the contribution of dust emission becomes important at longer wavelengths. However, in a small fraction of compact star-forming galaxies, the  $3.4 \mu\text{m} - 4.6 \mu\text{m}$  colour can be much higher, attaining values greater than 2 mag in some rare cases (Griffith et al. 2011; Izotov et al. 2011, 2014). This implies that the contribution of hot dust emission at  $3.4$  and  $4.6 \mu\text{m}$  in these galaxies is important and even dominant.

In Fig. 5, we present the spectral energy distribution of our galaxies including near- and mid-infrared ranges. Only two galaxies were detected by the *Wide-field Infrared Survey Explorer* (*WISE*). On the other hand, many galaxies from the comparison sample are detected by *WISE*, mainly because of their higher brightness (Fig. A7 – A9). The  $3.4 \mu\text{m}$  and  $4.6 \mu\text{m}$  fluxes in many galaxies from the comparison sample are consistent with the predictions of our modelled SEDs, if aperture corrections are taken into account. This implies that the contribution of emission from cool stars is small, indicating a relatively small mass of their population, at

least, inside the spectroscopic aperture. An indication of hot dust emission is present in some galaxies from the comparison sample, most notably in J120122 (Fig. A7c), J2238+1400 (Fig. A8m), J030321–075923 (Fig. A9a). We also note that the contribution of nebular continuum in the infrared range is high in all galaxies considered in this paper, most notably in J1248+4259 (Fig. 5g), where the nebular continuum starts dominating from  $\sim 5000\text{\AA}$ . Additionally, the presence of strong hydrogen and helium emission lines with very high equivalent widths in the near-infrared range will further alter the *J, H, K* magnitudes from those of the pure stellar emission, making difficult a stellar mass determination with the use of the near-infrared data.

In Fig. 6 we compare the carbon-to-oxygen abundance ratios derived from the matched spectra using the  $\text{O III}] \lambda 1666$  ( $(\text{C/O})_{\text{UV}}$ ) and  $[\text{O III}] \lambda 4959, 5007$  ( $(\text{C/O})_{\text{opt}}$ ) emission lines. The line  $\text{O III}] \lambda 1666$  is detected in all galaxies from Berg et al. (2016, 2019), in 6 LyC leaking galaxies, but almost not seen in the GP spectra from Ravindranath et al. (2020) and therefore they were



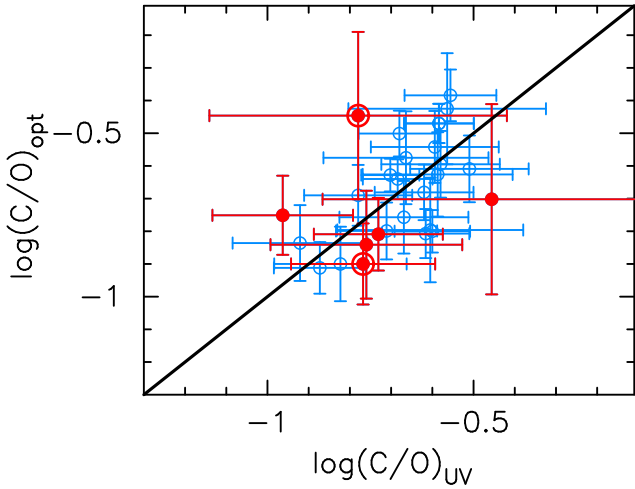


**Figure 6.** Comparison of the carbon-to-oxygen abundance ratios derived using  $\text{O III } \lambda 1666$  ( $(\text{C/O})_{\text{UV}}$ ) and  $[\text{O III}] \lambda 4959, 5007$  ( $(\text{C/O})_{\text{opt}}$ ) emission lines. Galaxies from Berg et al. (2016, 2019) and this paper are shown by blue open circles and filled red circles, respectively. Encircled symbols indicate the galaxies with  $f_{\text{esc}}(\text{LyC}) > 30$  per cent. The solid line is the line of equal values.

not used for a comparison. The figure shows a good agreement between the C/O abundance ratios derived by the two methods. This supports the reliability of the C/O abundance ratios derived using  $[\text{O III}] \lambda 4959, 5007$  emission lines.

#### 4 RELATIONS BETWEEN ABUNDANCES OF CNO ELEMENTS

To study the relations between the C/O, N/O and C/N abundance ratios with oxygen abundances  $12 + \log(\text{O}/\text{H})$  and stellar masses  $M_{\star}$  we use a sample of 42 galaxies including 11 LyC leaking galaxies at redshifts  $z \sim 0.3 - 0.4$  (this paper), 10 GP galaxies at redshifts  $z \sim 0.15 - 0.25$  (Ravindranath et al. 2020) and 21 galaxies at lower redshifts  $z \lesssim 0.04$  (Berg et al. 2016, 2019). All measurements of emission-line fluxes and determinations of element abundances have been done in this paper. In particular, we used the C/O abundance ratios derived from the  $\text{C III } \lambda 1908$  and  $[\text{O III}] \lambda 4959, 5007$  emission-line fluxes (Eq. 1).

In Fig. 7a we show the distribution in the  $12 + \log(\text{O}/\text{H}) - \log(\text{C}/\text{O})$  diagram of the LyC leaking galaxies (red symbols) and of the comparison sample (blue symbols). Here C/O abundance ratios are derived using non-scaled UV spectra. The LyC leaking galaxies J1154+2443, J1243+4646 and J1256+4509 with the escape fraction  $f_{\text{esc}}(\text{LyC}) > 30$  per cent (Table 1) are encircled. The green symbols in the figure also show the data for H II regions in our Galaxy (Esteban et al. 2002, 2009, 2014; García-Rojas & Esteban 2007; López-Sánchez et al. 2007), for which abundances were derived from the optical recombination carbon and oxygen lines. It is seen that there is no evident dependence of  $\log(\text{C}/\text{O})$  on  $12 + \log(\text{O}/\text{H})$  for the galaxies shown by red and blue symbols which have an average value  $-0.83 \pm 0.25$ , calculated in the range  $12 + \log(\text{O}/\text{H}) = 7.4 - 8.0$  (dashed line) with  $1\sigma$  dispersions (dotted lines). The derived average value is close to that obtained by Berg et al. (2016, 2019).

We suggest that the large dispersion for galaxies in Fig. 7a is due to that the UV and optical spectra of these galaxies are not well adjusted, i.e. the energy distribution in the UV spectra can not be

reproduced by the SEDs derived from the SDSS spectra (Figs. 3, A1, A3, A5).

The comparisons of the observed UV and optical spectra and photometric data with the modelled SEDs are presented in Figs. A1, A3, A5. Comparing these figures with Fig. 3 we note that photometric fluxes (magenta filled circles) from galaxies studied by Berg et al. (2016, 2019) are systematically higher than the spectroscopic fluxes in both the UV and optical ranges, indicating that angular sizes of these galaxies are larger than spectroscopic apertures. The agreement is better for the GP galaxies at higher redshifts from the Ravindranath et al. (2020) sample and is good for LyC leaking galaxies (Fig. 3).

Another feature is that the modelled SEDs fail to reproduce the energy distribution in the UV range in many galaxies from the Berg et al. (2016, 2019) and Ravindranath et al. (2020) samples. The agreement is better for LyC leaking galaxies (Fig. 3). To overcome this problem we scaled UV spectra to adjust them with the attenuated SEDs. The UV emission line intensities are also changed by the same factor.

Using scaled intensities in the optical range, we calculate  $\log(\text{C}/\text{O})$  in LyC leakers and in galaxies from the Berg et al. (2016, 2019) and Ravindranath et al. (2020) samples. Results of this correction are shown in Fig. 7b on the  $\log(\text{C}/\text{O}) - 12 + \log(\text{O}/\text{H})$  diagram. It is seen that the distribution of the galaxies is much tighter compared to that in Fig. 7a and all data are in much better agreement, showing no dependence of  $\log(\text{C}/\text{O})$  on the oxygen abundance at these low  $12 + \log(\text{O}/\text{H})$  values. This indicates a common carbon and oxygen origin. Although the average value of  $\log(\text{C}/\text{O}) = -0.75$  for galaxies with the oxygen abundances in the range 7.4–8.0 from the Berg et al. (2016, 2019) and Ravindranath et al. (2020) samples (dashed line) is similar to that in Fig. 7a, the dispersion is considerably reduced to the value of 0.13 dex. The distribution of the galaxies with modified  $\log(\text{C}/\text{O})$  values is in good agreement with the chemical evolution model by Carigi & Peimbert (2011) and, for Berg et al. (2016, 2019) data, above by 0.20 dex, compared to that for the galactic halo stars from Akerman et al. (2004) and Fabbian et al. (2009). On the other hand, the distribution of LyC leaking galaxies (red symbols) and GPs by Ravindranath et al. (2020) (blue crossed open circles) are in better agreement with the distribution of the halo stars.

The distribution of  $\log(\text{N}/\text{O})$  on oxygen abundance  $12 + \log(\text{O}/\text{H})$  is shown in Fig. 7c. Higher-redshift LyC leaking galaxies (this paper) and GPs by Ravindranath et al. (2020) have systematically higher, by a factor of  $\sim 2$ , N/O abundance ratios compared to lower-redshift galaxies from the Berg et al. (2016, 2019) samples. The latter galaxies likely do not show a dependence of the N/O ratio on oxygen abundance indicating a common origin of N and O at these metallicities. On the other hand, in LyC leakers (this paper) and GPs (Ravindranath et al. 2020), likely, an additional source of nitrogen nucleosynthesis is required, possibly, stellar winds from the most massive stars.

Finally, the distribution of galaxies in the  $\log(\text{C}/\text{N}) - 12 + \log(\text{O}/\text{H})$  diagram is shown in Fig. 7d. LyC leakers and GPs have considerably lower C/N abundance ratios compared to nearly constant values for galaxies at lower redshift and H II regions in the Milky Way. This appearance is presumably due to higher nitrogen abundances in LyC leakers and GPs, again favouring an additional mechanism of nitrogen production in higher-redshift galaxies.

We present in Fig. 8 the dependencies on the galaxy stellar mass  $M_{\star}$  of scaled C/O, N/O and C/N abundance ratios. The  $\log(\text{C}/\text{O})$  slightly declines with increasing  $M_{\star}$  (Fig. 8a) and this decline can

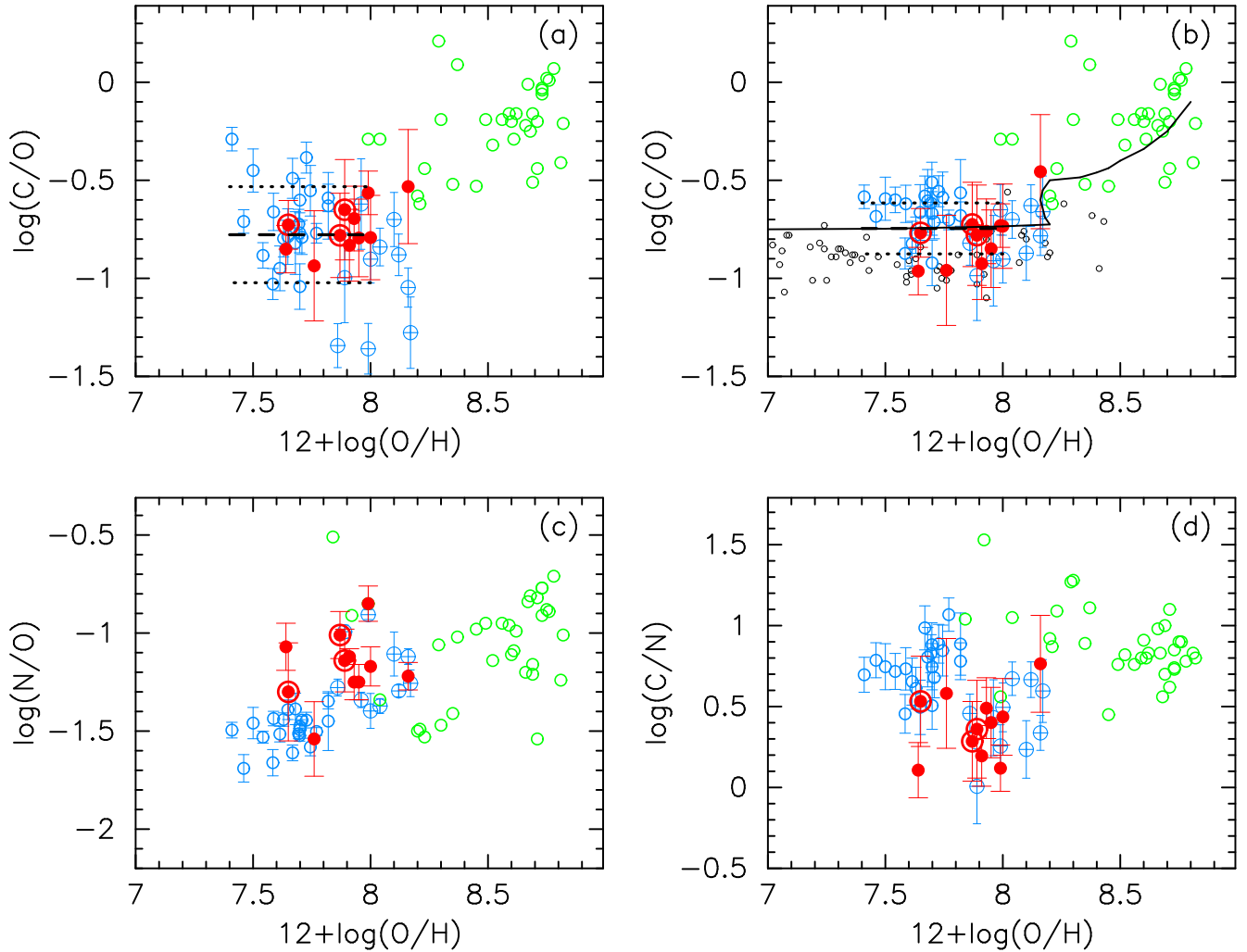


**Figure 7.** (a) The relation between the oxygen abundance  $12 + \log(\text{O}/\text{H})$  and  $\log(\text{C}/\text{O})$ . Carbon abundances are derived from the extinction-corrected  $\text{C III } \lambda 1908\text{\AA}$  emission line (red and blue symbols) and from the extinction-corrected recombination line  $\text{C II } \lambda 4267\text{\AA}$  (green symbols). No corrections to adjust UV and optical spectra were applied for galaxies, shown by blue symbols. (b) The same as in (a), but there is an adjustment to the UV spectra such that the optical and UV fluxes agree with SED models. (c) The relation  $12 + \log(\text{O}/\text{H})$  vs  $\log(\text{N}/\text{O})$ . (d) The relation  $12 + \log(\text{O}/\text{H})$  vs  $\log(\text{C}/\text{N})$ . The correction to adjust UV and optical spectra is applied. In all panels filled red circles are from this paper, open blue circles are from Berg et al. (2016, 2019), crossed open circles are from Ravindranath et al. (2020), and green symbols are from Esteban et al. (2002, 2009, 2014), García-Rojas & Esteban (2007), López-Sánchez et al. (2007). Small black open circles in (b) are halo stars (Akerman et al. 2004; Fabbian et al. 2009), black line is the chemical evolution model by Carigi & Peimbert (2011). Encircled symbols indicate the galaxies with  $f_{\text{esc}}(\text{LyC}) > 30$  per cent. Dashed lines in (a) and (b) indicate average  $\log(\text{C}/\text{O})$  for the galaxies with the oxygen abundances in the range 7.4 – 8.0, whereas dotted lines are  $1\sigma$  deviations from the average values.

be approximated by the maximum likelihood relation

$$\log\left(\frac{\text{C}}{\text{O}}\right) = -(0.040 \pm 0.023) \times \log\left(\frac{M_{\star}}{M_{\odot}}\right) - (0.410 \pm 0.185). \quad (7)$$

This relation together with  $1\sigma$  alternative relations are shown in Fig. 8a by solid and dotted lines, respectively. Previously a similar trend with a higher slope for a smaller sample in a smaller range of masses was noted by Berg et al. (2019) from the  $\log \text{C}/\text{O}$  – total baryonic mass diagram. It is shown in Fig. 8a by a dashed line. However, we note that a total baryonic mass relationship is not completely comparable to the stellar mass relationship.

We check whether the trend in Fig. 8a can be caused by the systematics in the determination of the carbon abundance. In particular, are the ionization correction factors (Fig. 2, Eq. 5) reliably take into account all stages of carbon ionization? For this, we consider a diagram  $\log(\text{C}/\text{O}) - \text{O}_{32}$  (Fig. 9). There is no trend in this

diagram, which implies that the applied  $\text{ICF}(\text{C}/\text{O})$  values are correct. We also note that the  $\text{C}/\text{O}$  abundance ratio in galaxies with  $f_{\text{esc}}(\text{LyC}) > 30$  per cent is not systematically different from that in other LyC leaking galaxies with lower  $f_{\text{esc}}(\text{LyC})$  and in galaxies from the comparison sample (see also Fig 7b).

The trend in Fig. 8a can also be attributed to a decreasing C and O effective yield with increasing stellar mass. More massive galaxies with  $M_{\star} \gtrsim 10^8 M_{\odot}$ , including LyC leaking galaxies (red symbols) and GPs by Ravindranath et al. (2020) (blue crossed open circles) have lower  $\log(\text{C}/\text{O})$  by  $\sim 0.2$  dex compared to the average value for lower-mass galaxies by Berg et al. (2016, 2019).

The  $\log(\text{N}/\text{O})$  for low-mass galaxies by Berg et al. (2016, 2019) is nearly constant, with an average value of  $\sim -1.5$  (Fig. 8b). On the other hand, the N/O ratio in higher-mass LyC leakers and GPs is not flat and enhanced by a factor of  $\sim 2$ , with an average  $\log(\text{N}/\text{O}) \sim -1.2$ . Similar enhanced  $\log(\text{N}/\text{O})$  was found in  $z = 2 - 3$  star-forming

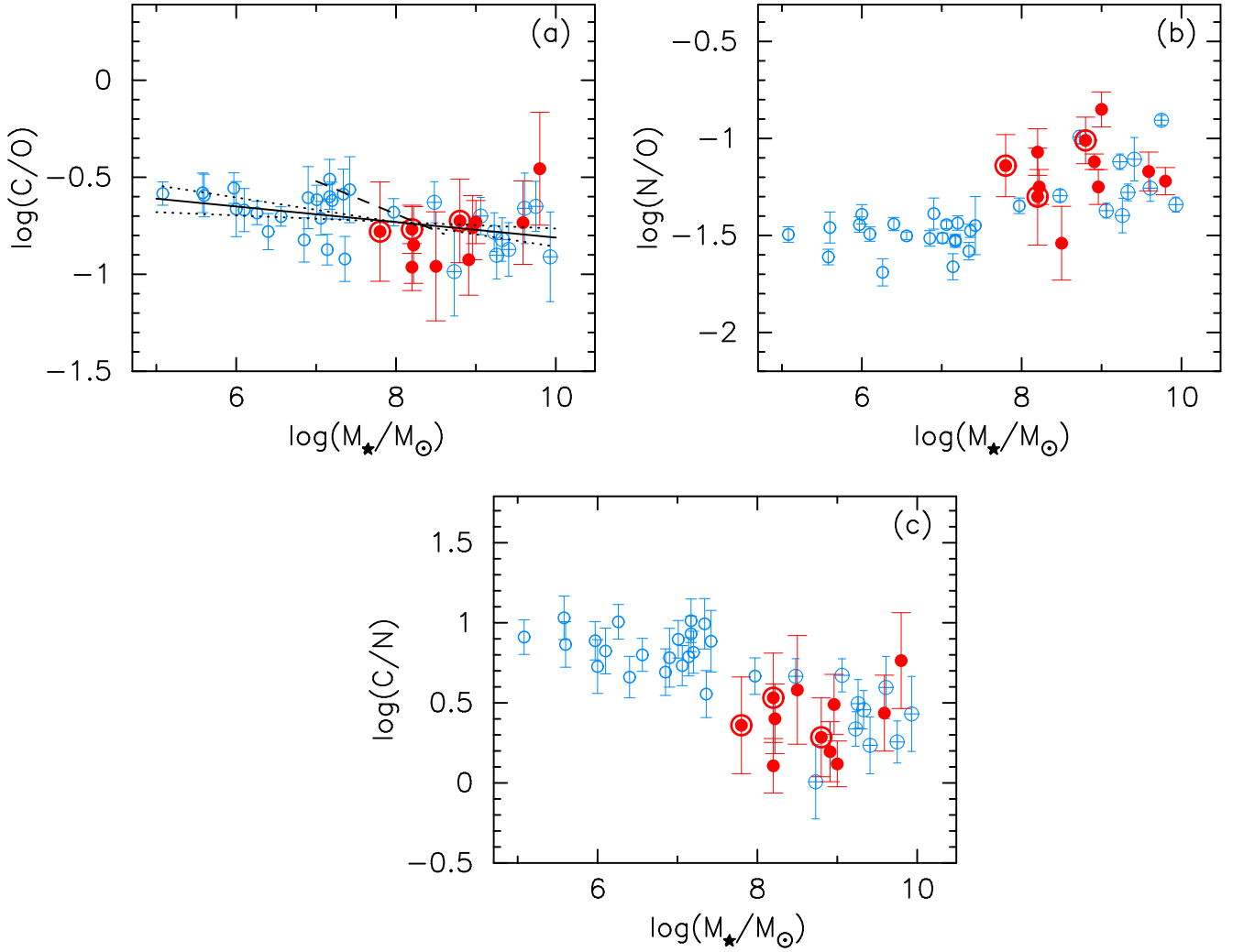


**Figure 8.** Relations between  $\log(M_{\star}/M_{\odot})$  and (a) scaled  $\log(C/O)$ , (b)  $\log(N/O)$  and (c)  $\log(C/N)$ . In (a) the most likelihood relation (Eq. 7) with  $1\sigma$  alternatives are shown by solid and dotted lines, respectively, whereas the relation between  $\log(C/O)$  and the baryonic mass by Berg et al. (2019) is represented with a dashed line. Symbols are the same as in Fig. 7.

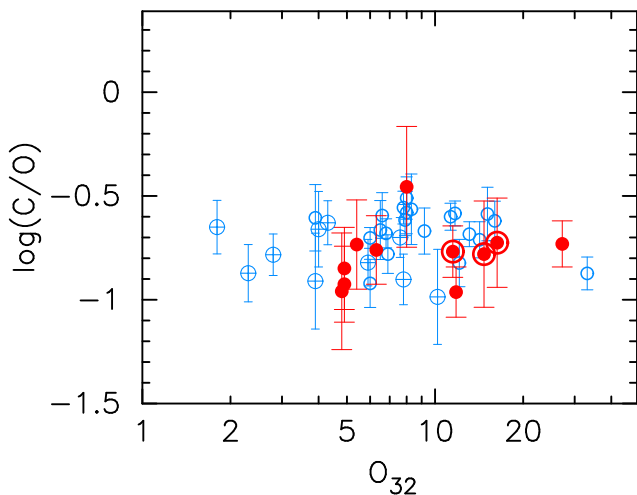


**Figure 9.** The relation between  $\log(C/O)$ , derived from C III]  $\lambda 1908$  and [O III]  $\lambda 4959$ , 5007 emission-line fluxes, and  $O_{32} = [O III] \lambda 5007 / [O II] \lambda 3727$ . Symbols are the same as in Fig. 7.

galaxies with similar stellar masses, oxygen abundances and excitation characteristics of their H II regions (strength of emission lines and  $O_{32}$ ) (Steidel et al. 2014; Shapley et al. 2015; Strom et al. 2017). Correspondingly, the  $\log(C/N)$  in higher-mass LyC leakers and GPs is  $\sim 0.5$  dex lower than in low-mass galaxies from Berg et al. (2016, 2019). The transition in properties from low- to high-mass galaxies occurs at  $M_{\star} \sim 10^8 M_{\odot}$  (Fig. 8c).

In the light of findings in this paper, a successful model of carbon, nitrogen and oxygen origin in dwarf star-forming galaxies should reproduce all trends of C/O, N/O and C/N abundance ratios with oxygen abundance and stellar mass, namely, 1) the constancy of the C/O abundance ratio (Fig. 7b) with oxygen abundance, the N/O jump up and the C/N jump down at  $12 + \log(O/H) \gtrsim 7.8$  (Figs. 7c and 7d), and 2) the steady decrease of the C/O abundance ratio with  $M_{\star}$  (Fig. 8a), the N/O jump up and C/N jump down at  $M_{\star} \gtrsim 10^8 M_{\odot}$  (Figs. 8b and 8c).

Various mechanisms of the C/O and N/O evolution were considered in the past. In general, oxygen is produced by massive stars whereas carbon is a primary element produced by massive and intermediate-mass stars. Nitrogen is produced mainly in the intermediate-mass stars, as a primary element at low metallicities

and as a secondary element at high metallicities. For example, [Henry et al. \(2000\)](#) have shown that both C/O and N/O abundance ratios steadily increase with oxygen abundance. It was shown by e.g. [Pilyugin \(1992, 1993\)](#), [Henry et al. \(2000\)](#), [Yin, Matteucci & Vladilo \(2011\)](#), [Berg et al. \(2016, 2019\)](#) that bursty models in dwarf galaxies (either closed-box or with the loss of synthesized oxygen via galactic winds) are able to reproduce the temporal evolution and the spread of C/O and N/O abundance ratios. The nitrogen enhancement via local pollution of the ISM by massive O and WR stars was also considered (e.g. [Henry et al. 2000](#); [Izotov et al. 2006](#)). In particular, [Izotov et al. \(2006\)](#) have suggested that the observed high N/O abundance ratio is not characteristic of the entire H II region, but rather of dense nitrogen-enriched clumps expelled by Wolf-Rayet stars. In general, in all these models both the C/O and N/O abundance ratios increase with increasing  $12 + \log(\text{O}/\text{H})$ , which does not exactly agree with our data.

The relation  $M_{\star} - \log(\text{C}/\text{O})$  in Fig. 8a, at least in part, may be caused by decreasing efficiency of the galactic wind expelling oxygen from the galaxy in higher-mass galaxies with higher gravitational potentials.

Our data indicate that there is an additional source of nitrogen enrichment, possibly stellar winds from the most massive stars in more massive galaxies. Some indication of this is found by [Izotov et al. \(2018b\)](#) who noted that strong O VI  $\lambda 1035$  stellar line with P Cygni profile is detected in almost all LyC leakers shown by red symbols. This implies that massive stars with masses above  $100 M_{\odot}$  are present in these galaxies. On the other hand, the O VI line is almost not seen in galaxies with  $M_{\star} < 10^8 M_{\odot}$  ([Izotov et al. 2021](#)) with similarly young starburst ages. Thus, likely, the IMF in more massive galaxies extends to stars with higher masses, which more likely can go through the phase with stellar wind, including the Wolf-Rayet stage, and enrich the interstellar medium with nitrogen. Unfortunately, we can not prove this statement, because the redshifts of low-mass galaxies from the sample by [Berg et al. \(2016, 2019\)](#) are too low for observation of the O VI  $\lambda 1035$  at present.

## 5 CONCLUSIONS

We present new *Hubble Space Telescope (HST)*/Space Telescope Imaging Spectrograph (STIS) observations of eleven  $z \sim 0.3 - 0.4$  Lyman continuum (LyC) leaking galaxies from the sample by [Izotov et al. \(2016a,b, 2018a,b\)](#). We use these data in combination with optical Sloan Digital Sky Survey (SDSS) observations to study the abundances of CNO elements and relations between them. These data were supplemented by the archival *HST* STIS and Cosmic Origins Spectrograph (COS) observations of the C III]  $\lambda 1908\text{\AA}$  emission line, together with available SDSS spectra of low-redshift dwarf galaxies, totalling in a sample of 42 galaxies. Our main results are summarised as follows:

1. The continua of all 11 LyC-leaking galaxies in the UV spectra can be reproduced by extrapolation of the spectral energy distributions (SEDs) which are modelled using the SDSS optical spectra. This implies that a) the spectra in the UV and optical ranges are well adjusted. Their fluxes are in agreement with *Galaxy Evolution Explorer (GALEX)* and SDSS photometric fluxes and therefore only small aperture corrections are needed to compare data in these ranges and b) emission in the UV and optical ranges is almost totally produced by the stars formed in the same young burst of star formation.

2. For many other galaxies selected from the literature, the UV and optical spectroscopic fluxes are considerably lower than the

fluxes obtained from the *GALEX* and SDSS photometry, meaning that the angular sizes of galaxies are larger than the spectroscopic apertures in both the UV and optical ranges. Furthermore, in many of these galaxies the continua in the UV range cannot be reproduced by extrapolation of the SED modelled for SDSS spectra. In these cases we adopt scaling factors in order to fit both the UV and optical spectra by the same SED modelled for the SDSS spectrum, assuming that emission in both ranges is produced by the stars formed during the same young burst of star formation.

3. Both the UV and optical data are corrected for extinction which is derived from the hydrogen Balmer decrement. The carbon abundance is derived from the C III]  $\lambda 1908\text{\AA}$  emission line measured in the STIS or COS spectra, whereas nitrogen and oxygen abundances are obtained from the [N II]  $\lambda 6584\text{\AA}$  and [O II]  $\lambda 3727\text{\AA}$ , [O III]  $\lambda 4959\text{\AA}$ ,  $\lambda 5007\text{\AA}$  emission lines, respectively, measured in the SDSS spectra. Adopting the method of SED fitting that consistently reproduces the UV and optical spectra, we considerably reduce (by a factor of  $\sim 2$ ) the dispersion in  $\log(\text{C}/\text{O})$ . We find that  $\log(\text{C}/\text{O})$  at low oxygen abundances  $12 + \log(\text{O}/\text{H}) \lesssim 8.0$  is constant with an average value of  $-0.75 \pm 0.13$  for the total sample of selected galaxies. This implies a common origin of oxygen and carbon. The LyC leakers and “green peas” (GP) studied by [Ravindranath et al. \(2020\)](#) are shifted in the  $\log(\text{C}/\text{O}) - 12 + \log(\text{O}/\text{H})$  diagram to lower values of  $\log(\text{C}/\text{O})$  by  $\sim 0.10 - 0.15$  dex. The N/O abundance ratio in LyC leakers and GPs is  $\sim 2$  higher than that of the rest of the sample. This results in a factor of  $\sim 3$  lower C/N ratio in the LyC leakers and GPs compared to other selected galaxies.

4. We find a trend of decreasing  $\log(\text{C}/\text{O})$  with increasing stellar mass  $M_{\star}$ . In this relation, the LyC leakers and GPs are located at the high-mass end of the diagram with  $M_{\star} \gtrsim 10^8 M_{\odot}$ . A similar trend, but with a higher slope, has been obtained by [Berg et al. \(2019\)](#) for a smaller sample with a smaller range of masses. The N/O abundance ratio in low-mass galaxies with  $M_{\star} \lesssim 10^8 M_{\odot}$  is constant with  $\log(\text{N}/\text{O}) \sim -1.5$ , indicating a primary origin for nitrogen. The N/O abundance ratio in higher-mass LyC leakers and GPs is enhanced by a factor of  $\sim 2$  to higher values, indicating an additional source of nitrogen enrichment.

5. We speculate that the observed abundance ratios and the transition of N/O abundance ratio from low values in low-mass galaxies to higher values at  $\gtrsim 10^8 M_{\odot}$  could be due to different stellar IMFs which extend to higher masses of massive stars in higher-mass galaxies. We also discuss alternate explanations and conclude that the origin of the enhanced N/O abundances in some of LyC leakers (cf. [Guseva et al. 2020](#)) and GPs remains unexplained.

## ACKNOWLEDGEMENTS

Based on observations made with the NASA/ESA *Hubble Space Telescope*, obtained from the data archive at the Space Telescope Science Institute. STScI is operated by the Association of Universities for Research in Astronomy, Inc. under National Aeronautics and Space Administration (NASA) contract NAS 5-26555. Support for this work was provided by NASA through grant number HST-GO-15941.002-A from the Space Telescope Science Institute, which is operated by Association of Universities for Research in Astronomy (AURA), Inc., under NASA contract NAS 5-26555. Y.I. acknowledges support from the National Academy of Sciences of Ukraine (Project “The matter properties at high energies and in galaxies during the reionization of the Universe”) and from the Simons Foundation. Funding for Sloan Digital Sky Survey-III (SDSS-III) has been provided by the Alfred P. Sloan Foundation, the Participating



Institutions, the National Science Foundation, and the U.S. Department of Energy Office of Science. The SDSS-III web site is <http://www.sdss3.org/>. SDSS-III is managed by the Astrophysical Research Consortium for the Participating Institutions of the SDSS-III Collaboration. *Galaxy Evolution Explorer (GALEX)* is a NASA mission managed by the Jet Propulsion Laboratory. This research has made use of the NASA/Infrared Processing and Analysis Center (IPAC) Extragalactic Database (NED) which is operated by the Jet Propulsion Laboratory, California Institute of Technology, under contract with the National Aeronautics and Space Administration. This publication makes use of data products from the *Wide-field Infrared Survey Explorer (WISE)*, which is a joint project of the University of California, Los Angeles, and the Jet Propulsion Laboratory, California Institute of Technology, funded by the National Aeronautics and Space Administration.

#### DATA AVAILABILITY

The data underlying this article will be shared on reasonable request to the corresponding author.

#### REFERENCES

- Akerman C. J., Carigi L., Nissen P. E., Pettini M., Asplund M., 2004, *A&A*, 414, 931
- Aller L. H., 1984, *Physics of Thermal Gaseous Nebulae*. Dordrecht: Reidel
- Berg D. A., Skillman E. D., Henry R. B. C., Erb D. K., Carigi L., 2016, *ApJ*, 827, 126
- Berg D. A., Erb D. K., Henry R. B. C., Skillman E. D., McQuinn K. B. W., 2019, *ApJ*, 874, 93
- Berg D. A., Pogge R. W., Skillman E. D., Croxall K. V., Moustakas J., Rogers N. S. J., Sun J., 2020, *ApJ*, 893, 96
- Cardelli J. A., Clayton G. C., Mathis J. S., 1989, *ApJ*, 345, 245
- Carigi L., Peimbert M., 2011, *Rev. Mex. Astron. Astrofis.*, 47, 139
- Erb D. K., Pettini M., Shapley A. E., Steidel C. C., Law D. R., Reddy N. A., 2010, *ApJ*, 719, 1168
- Esteban C., Peimbert M., Torres-Peimbert S., Rodríguez M., 2002, *ApJ*, 581, 241
- Esteban C., Bresolin F., Peimbert M., García-Rojas J., Peimbert A., Mesa-Delgado A., 2009, *ApJ*, 700, 654
- Esteban C., García-Rojas J., Carigi L., Peimbert M., Bresolin F., López-Sánchez A. R., Mesa-Delgado A., 2014, *MNRAS*, 443, 624
- Fabbian D., Nissen P. E., Asplund M., Pettini M., Akerman C., 2009, *A&A*, 500, 1143
- Ferland G. J. et al., 2013, *Rev. Mex. Astron. Astrofis.*, 49, 137
- García-Rojas J., Esteban C., 2007, *ApJ*, 670, 457
- Garnett D. R., Skillman E. D., Dufour R. J., Peimbert M., Torres-Peimbert S., Terlevich R., Terlevich E., Shields G. A., 1995, *ApJ*, 443, 64
- Griffith R. L. et al. 2011, *ApJ*, 736, L22
- Guseva N. G. et al., 2020, *MNRAS*, 497, 4293
- Henry R. B. C., Edmunds M. G., Köppen J., 2000, *ApJ*, 541, 660
- Izotov Y. I., Thuan T. X., 1999, *ApJ*, 511, 639
- Izotov Y. I., Thuan T. X., Lipovetsky V. A., 1994, *ApJ*, 435, 647
- Izotov Y. I., Stasińska G., Meynet G., Guseva N. G., Thuan T. X., 2006, *A&A*, 448, 955
- Izotov Y. I., Guseva N. G., Fricke K. J., Henkel C., 2011, *A&A*, 536, L7
- Izotov Y. I., Guseva N. G., Fricke K. J., Henkel C., 2011, *A&A*, 561, 33
- Izotov Y. I., Orlitová I., Schaerer D., Thuan T. X., Verhamme A., Guseva N. G., Worseck G., 2016a, *Nature*, 529, 178
- Izotov Y. I., Schaerer D., Thuan T. X., Worseck G., Guseva N. G., Orlitová I., Verhamme A., 2016b, *MNRAS*, 461, 3683
- Izotov Y. I., Schaerer D., Worseck G., Guseva N. G., Thuan T. X., Verhamme A., Orlitová I., Fricke K. J., 2018a, *MNRAS*, 474, 4514

- Izotov Y. I., Worseck G., Schaerer D., Guseva N. G., Thuan T. X., Fricke K. J., Verhamme A., Orlitová I., 2018b, *MNRAS*, 478, 4851
- Izotov Y. I., Worseck G., Schaerer D., Guseva N. G., Chisholm J., Thuan T. X., Fricke K. J., Verhamme A., 2021, *MNRAS*, 503, 1734
- Llerena et al., 2022, *A&A*, 659, A16
- López-Sánchez Á. R., Esteban C., García-Rojas J., Peimbert M., Rodríguez M., 2007, *ApJ*, 656, 168
- Pilyugin L. S., 1992, *A&A*, 260, 58
- Pilyugin L. S., 1993, *A&A*, 277, 42
- Ravindranath S., Monroe T., Jaskot A., Ferguson H. C., Tumlinson J., 2020, *ApJ*, 896, 170
- Schaerer D., Izotov Y. I., Nakajima K., Worseck G., Chisholm J., Verhamme A., Thuan T. X., de Barros S., 2018, *A&A*, 616, L14
- Schaerer D. et al., 2022, *A&A*, 658, L11
- Senchyna P. et al., 2017, *MNRAS*, 472, 2608
- Shapley A. E. et al., 2015, *ApJ*, 801, 88
- Steidel C. C. et al., 2014, *ApJ*, 795, 165
- Strom A. L., Steidel C. C., Rudie G. C., Trainor, R. F., Pettini M., Reddy N. A., 2017, *ApJ*, 836, 164
- Thuan T. X., Izotov Y. I., Foltz C. B., 1999, *ApJ*, 525, 105
- Yin J., Matteucci F., Vladilo G., 2011, *A&A*, 531, 136

#### APPENDIX A: SED FITS OF GALAXIES SPECTRA FROM THE LITERATURE

#### APPENDIX B: CHARACTERISTICS FOR THE DETERMINATION OF THE C/O ABUNDANCE RATIOS

This paper has been typeset from a  $\text{\LaTeX}$  file prepared by the author.

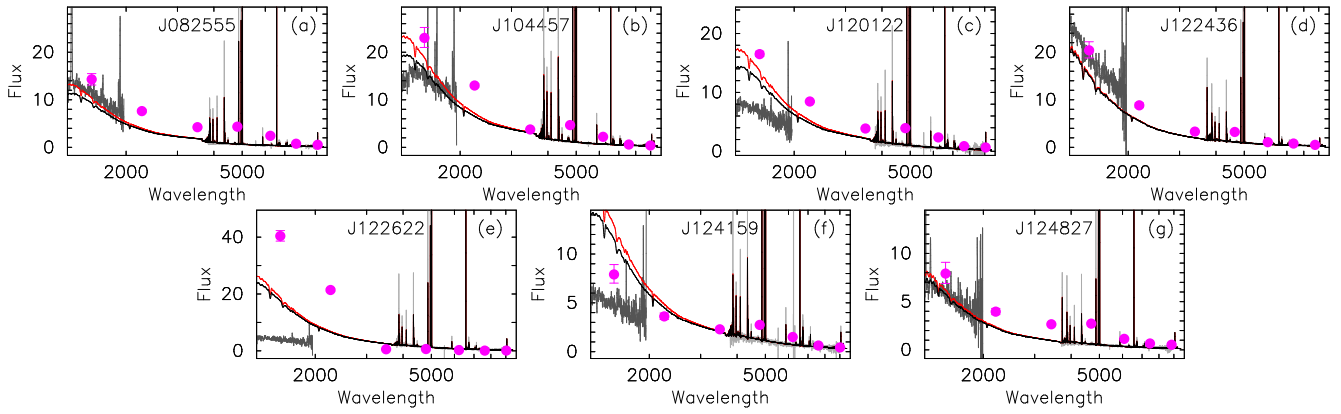


**Figure A1.** The same as in Fig. 3 but for galaxies from Berg et al. (2016).

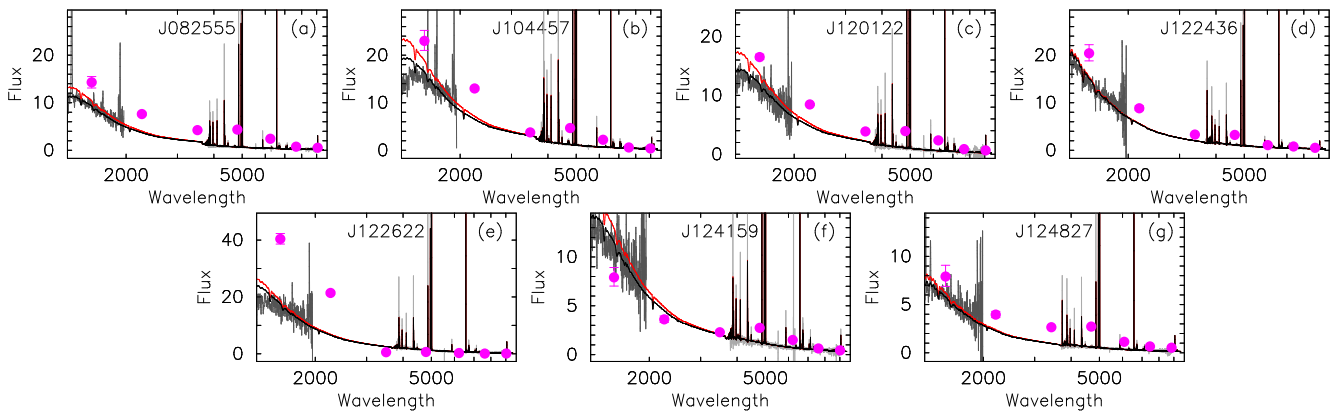


**Figure A2.** The same as in Fig. 4 but for galaxies from Berg et al. (2016).

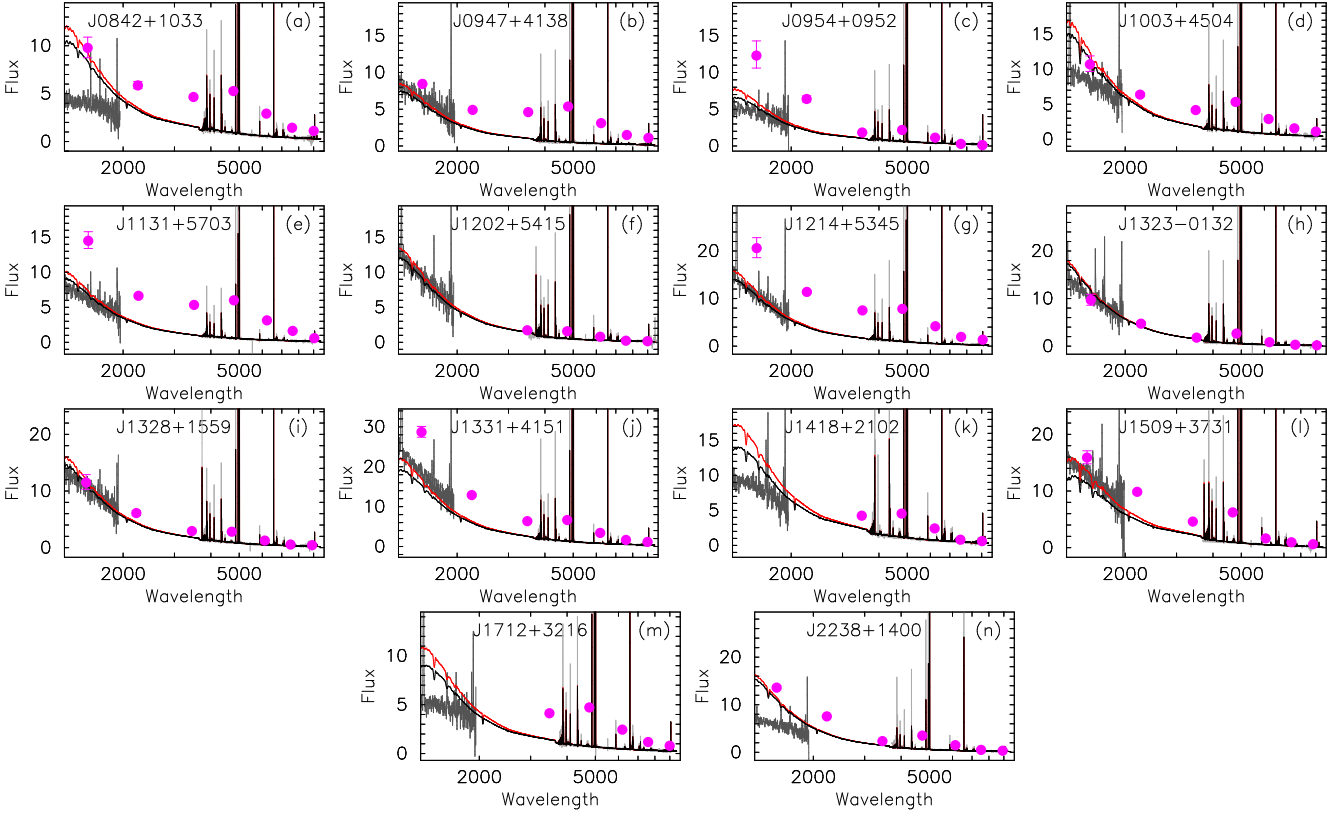


Figure A3. The same as in Fig. 3 but for galaxies from Berg et al. (2019).

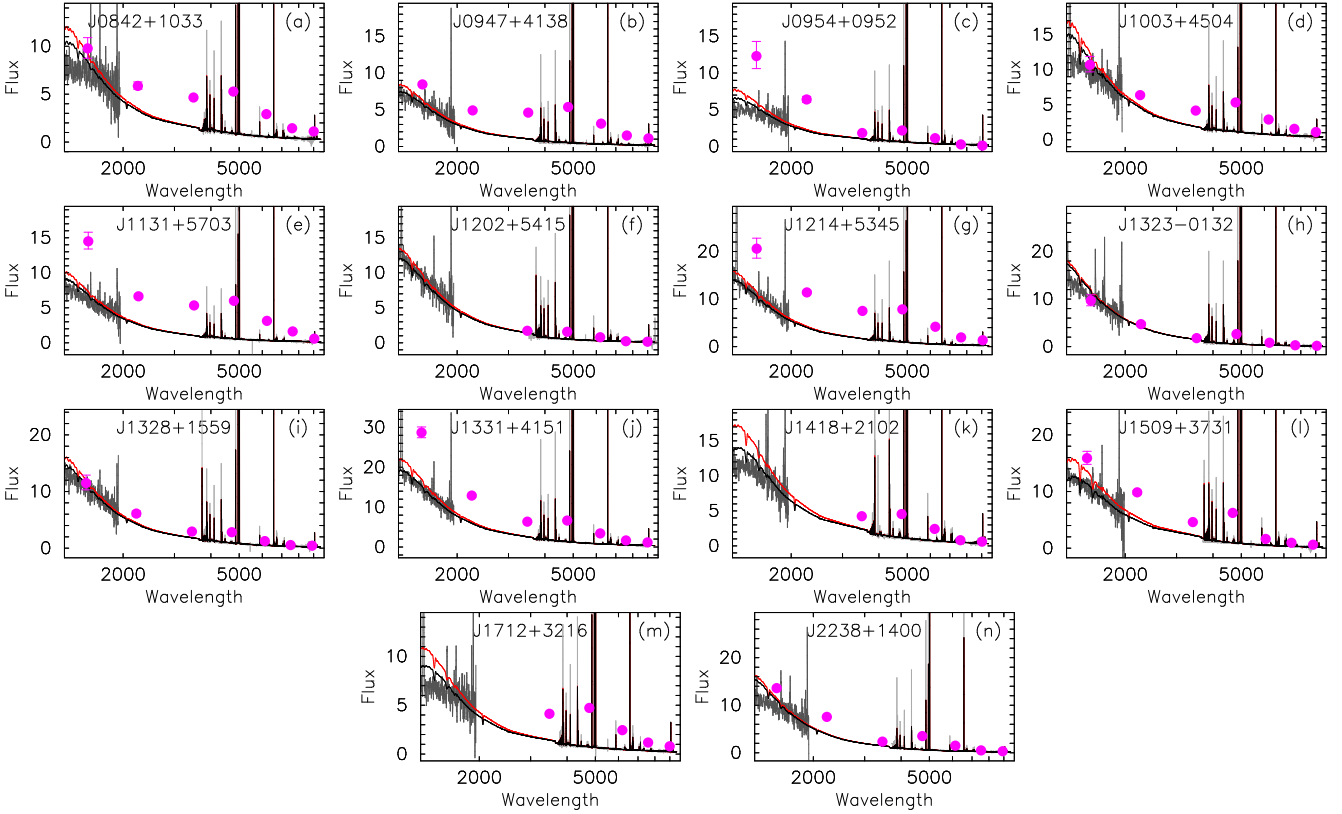
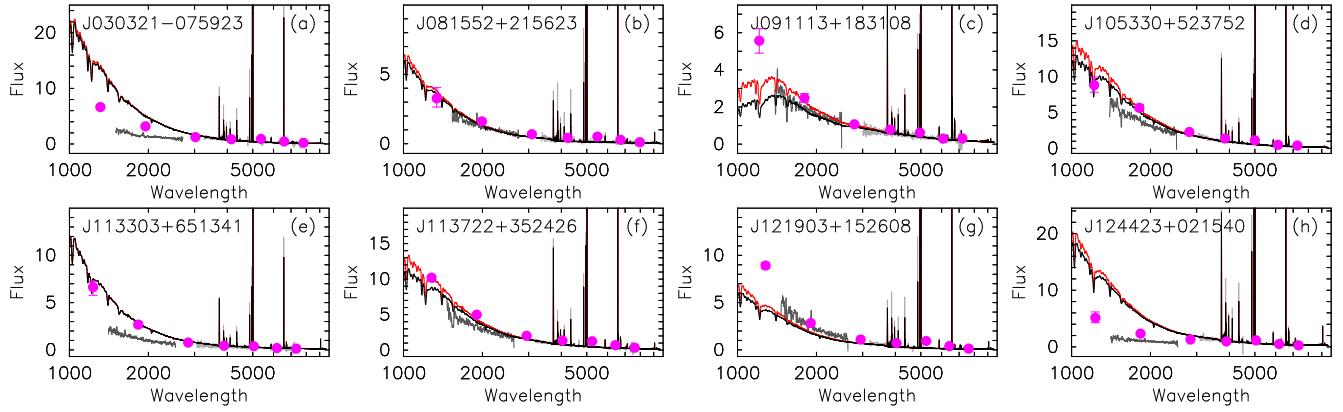
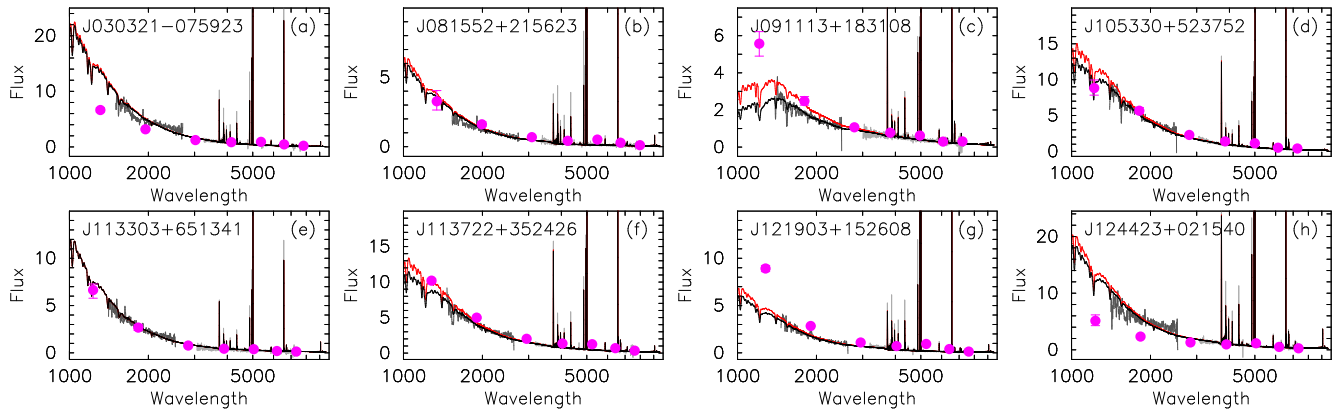


Figure A4. The same as in Fig. 4 but for galaxies from Berg et al. (2019).



**Figure A5.** The same as in Fig. 3 but for galaxies from Ravindranath et al. (2020).



**Figure A6.** The same as in Fig. 4 but for galaxies from Ravindranath et al. (2020).

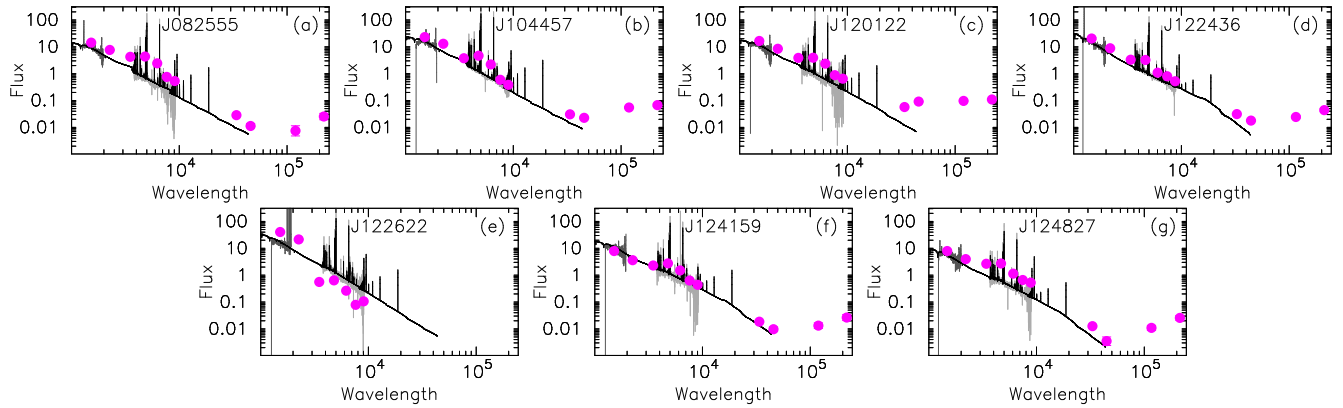


**Figure A7.** The same as in Fig. 5 but for galaxies from Berg et al. (2016). Stellar and nebular SEDs are not shown.



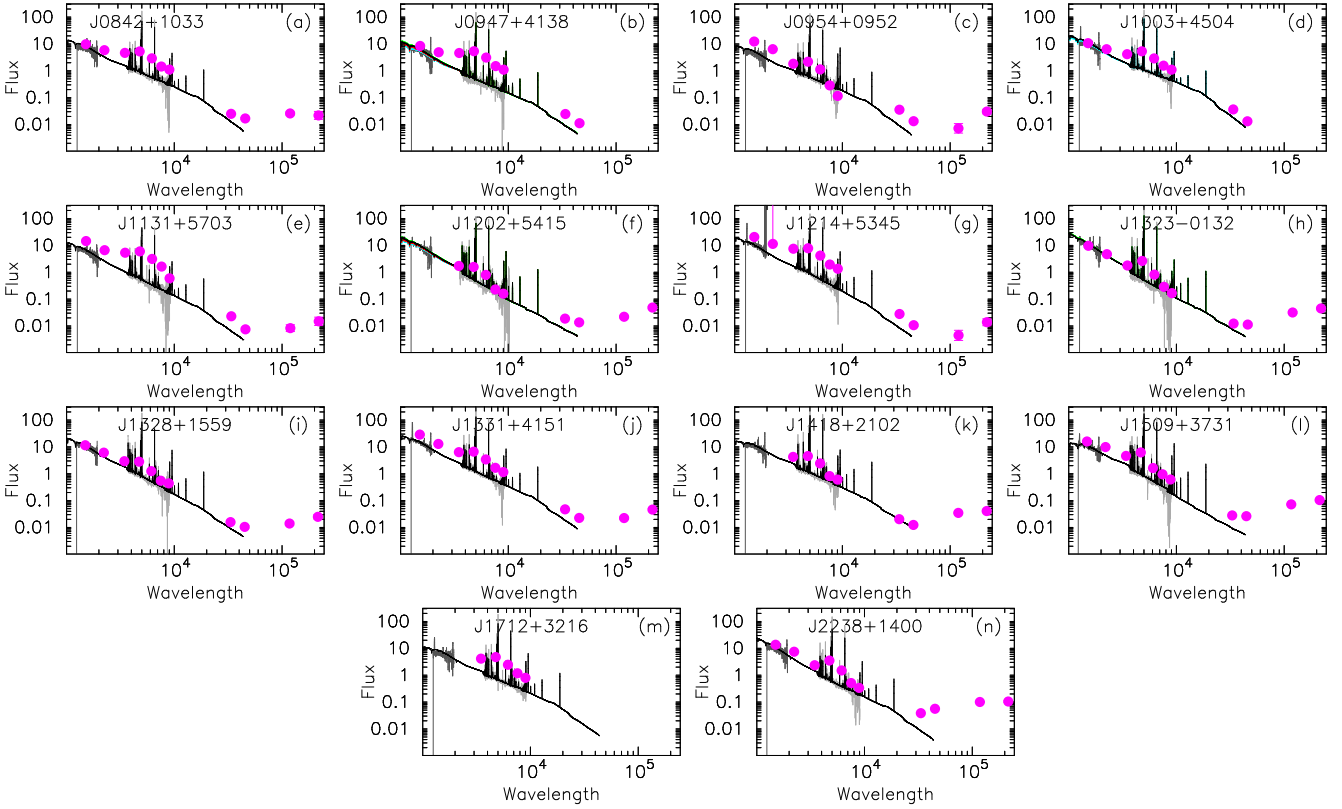


**Figure A8.** The same as in Fig. 5 but for galaxies from Berg et al. (2019). Stellar and nebular SEDs are not shown.

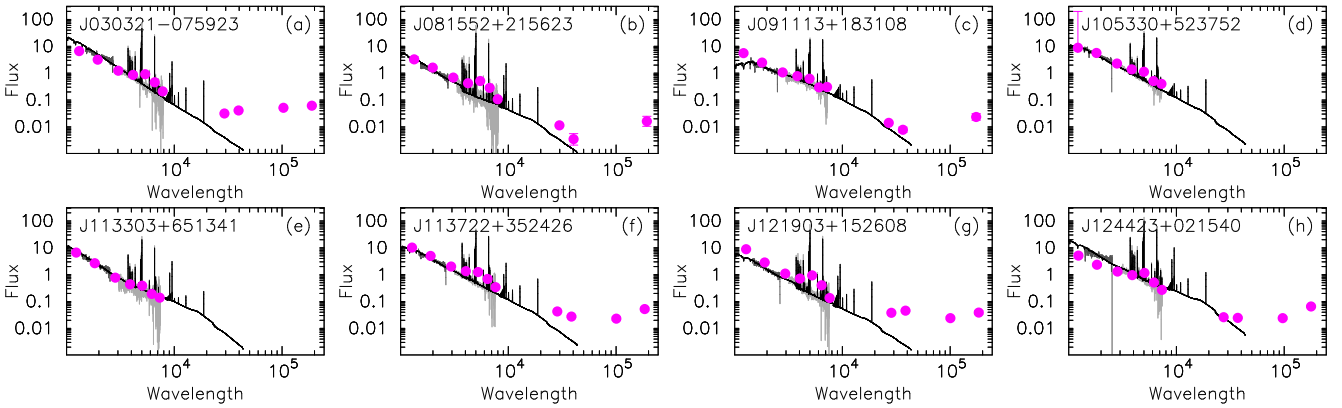


**Figure A9.** The same as in Fig. 5 but for galaxies from Ravindranath et al. (2020). Stellar and nebular SEDs are not shown.

**Table B1.** Characteristics for the determination of the C/O abundance ratio in galaxies from [Berg et al. \(2016\)](#)

Name	$F^a$ (C III] $\lambda 1908$ )	EW <sup>b</sup> (C III] $\lambda 1908$ )	$F^a$ (O III] $\lambda 1666$ )	EW <sup>b</sup> (O III] $\lambda 1666$ )	$F^a$ (H $\beta$ ) $\lambda 4861$ )	EW <sup>b</sup> (H $\beta$ ) $\lambda 4861$ )	$C_{\text{int}}^c$ (H $\beta$ ) $\lambda 4861$ )	$C_{\text{int}}^c$ (C III] $\lambda 1908$ )	$C_{\text{int}}^c$ (O III] $\lambda 1666$ )	corr. <sup>d</sup>
J082555	133.4±16.0	16.7±2.0	35.3±16.0	3.6±1.6	168.8±2.1	254±3	0.148±0.027	0.354±0.064	0.365±0.067	0.820
J104457	186.2±16.1	16.8±1.5	75.6±16.0	6.3±1.3	307.0±2.7	285±2	0.176±0.027	0.421±0.065	0.437±0.067	1.000
J120122	59.2±16.0	15.7±4.2	16.0±16.0	3.0±3.0	188.2±1.1	201±1	0.176±0.027	0.421±0.065	0.437±0.067	1.667
J124159	42.4± 8.0	12.7±2.4	18.1± 8.0	5.0±2.2	145.4±1.0	130±1	0.150±0.028	0.359±0.067	0.370±0.069	2.222
J122622	32.1± 3.2	10.5±1.0	10.1± 3.2	3.2±1.0	181.6±1.0	154±1	0.084±0.027	0.201±0.065	0.207±0.067	4.000
J122436	111.8± 4.2	9.6±0.4	25.6± 4.1	1.8±0.3	108.3±1.9	116±2	0.024±0.028	0.057±0.068	0.059±0.069	0.741
J124827	54.7± 6.0	14.6±1.6	55.3± 6.0	2.4±0.3	54.7±1.4	111±3	0.088±0.031	0.211±0.074	0.217±0.076	0.909

Name	$t(\text{O III})^e$	$I(\lambda)/I(\text{H}\beta)^f$	$12+\log(\text{O}/\text{H})$	$\log(\text{C}/\text{O})_{\text{opt}}^g$	$\log(\text{C}/\text{O})_{\text{UV}}^h$			
	(C III] $\lambda 1908$ )	(O III] $\lambda 1666$ ) ([O II] $\lambda 3727$ ) ([O III] $\lambda 5007$ )						
J082555	1.89±0.06	1.042±0.125	0.283±0.128	0.309±0.014	3.614±0.075	7.41±0.01	-0.584±0.060	-0.470±0.085
J104457	1.96±0.05	1.066±0.052	0.446±0.052	0.331±0.011	4.336±0.089	7.46±0.01	-0.684±0.060	-0.640±0.085
J120122	1.76±0.05	0.922±0.249	0.257±0.069	0.539±0.012	3.559±0.075	7.50±0.01	-0.594±0.110	-0.542±0.155
J124159	1.64±0.05	1.048±0.198	0.459±0.203	1.182±0.008	4.610±0.098	7.68±0.01	-0.605±0.160	-0.796±0.226
J122622	1.63±0.04	0.926±0.277	0.295±0.093	0.929±0.020	5.576±0.116	7.77±0.01	-0.702±0.050	-0.628±0.071
J122436	1.55±0.05	0.821±0.031	0.192±0.032	0.821±0.024	5.550±0.120	7.82±0.01	-0.680±0.070	-0.501±0.099
J124827	1.59±0.07	1.219±0.133	0.252±0.027	0.733±0.026	6.049±0.133	7.82±0.01	-0.564±0.170	-0.425±0.240

<sup>a</sup>Observed flux in  $10^{-16}$  erg  $\text{s}^{-1}$   $\text{cm}^{-2}$ .<sup>b</sup>Restframe equivalent width in Å.<sup>c</sup>Extinction coefficient for H $\beta$ , C III]  $\lambda 1908$  and O III]  $\lambda 1666$  emission lines.<sup>d</sup>Correction factor used to adjust observed UV spectrum with the modelled SED.<sup>e</sup> $t(\text{O III}) = T_e(\text{O III})/10^4\text{K}$ , where  $T_e(\text{O III})$  is the electron temperature in  $\text{O}^{2+}$  zone derived by the direct method.<sup>f</sup>Extinction-corrected flux ratios.<sup>g</sup>C/O abundance ratio is derived using C III]  $\lambda 1908$  and [O III]  $\lambda 4959, 5007$  emission-line fluxes.<sup>h</sup>C/O abundance ratio is derived using C III]  $\lambda 1908$  and O III]  $\lambda 1666$  emission-line fluxes.

**Table B2.** Characteristics for the determination of the C/O abundance ratio in galaxies from Berg et al. (2019)

Name	$F^a$ (C III] $\lambda 1908$ )	EW <sup>b</sup> (C III] $\lambda 1908$ )	$F^a$ (O III] $\lambda 1666$ )	EW <sup>b</sup> (O III] $\lambda 1666$ )	$F^a$ (H $\beta$ $\lambda 4861$ )	EW <sup>b</sup> (H $\beta$ $\lambda 4861$ )	$C_{\text{int}}^c$ (H $\beta$ $\lambda 4861$ )	$C_{\text{int}}^c$ (C III] $\lambda 1908$ )	$C_{\text{int}}^c$ (O III] $\lambda 1666$ )	corr. <sup>d</sup>
J084236	28.9±12.0	13.3±5.5	20.1±12.0	6.1±6.1	106.2±1.8	150±3	0.128±0.028	0.306±0.067	0.316±0.069	1.812
J094718	80.2±16.0	22.0±4.4	14.8±16.0	2.7±2.9	89.6±1.5	219±4	0.116±0.029	0.278±0.070	0.286±0.072	0.897
J095430	51.9± 8.0	23.6±3.6	23.8± 8.0	6.7±2.3	83.9±1.6	153±3	0.150±0.029	0.359±0.069	0.370±0.072	1.000
J100348	66.9± 8.0	14.7±1.8	23.7± 8.0	3.7±1.2	98.2±1.8	100±2	0.108±0.029	0.258±0.069	0.266±0.074	1.177
J113116	49.5± 6.4	10.0±1.3	14.1± 6.4	2.8±1.3	61.0±1.4	124±3	0.092±0.030	0.220±0.072	0.227±0.074	1.000
J120202	69.1± 7.2	12.4±1.3	27.5± 7.2	3.9±1.0	140.2±2.0	292±4	0.100±0.028	0.239±0.067	0.247±0.069	1.000
J121402	107.7± 6.5	16.6±1.0	34.1± 6.4	3.9±0.7	119.3±1.9	130±2	0.112±0.028	0.268±0.067	0.276±0.069	1.000
J132347	88.0± 8.8	17.1±1.7	76.5± 8.8	10.2±1.2	137.9±1.0	256±2	0.032±0.028	0.077±0.067	0.079±0.069	1.000
J132853	50.5±12.8	6.7±1.7	25.3±12.8	3.1±1.6	132.5±2.0	171±3	0.084±0.032	0.201±0.077	0.207±0.079	1.000
J133126	163.5±16.1	15.7±1.5	80.5±16.0	5.8±1.2	182.9±2.3	158±2	0.128±0.027	0.306±0.065	0.316±0.067	0.800
J141851	126.7± 6.9	24.5±1.4	70.0± 6.8	10.9±1.1	244.2±2.7	228±3	0.204±0.027	0.488±0.065	0.503±0.067	1.250
J150934	121.1±12.1	15.3±1.5	54.9±12.0	5.6±1.2	190.1±2.4	237±3	0.220±0.027	0.526±0.067	0.542±0.067	0.833
J171236	55.1± 8.0	18.6±2.7	27.2± 8.0	7.1±2.1	108.6±1.7	179±3	0.175±0.031	0.419±0.074	0.431±0.076	1.333
J223831	48.5± 8.2	19.9±3.3	21.8± 8.1	4.2±1.5	87.6±1.6	185±4	0.052±0.030	0.124±0.072	0.128±0.074	1.667

Name	$t(\text{O III})^e$	$I(\lambda)/I(\text{H}\beta)^f$	$12+\log(\text{O}/\text{H})$	$\log(\text{C}/\text{O})_{\text{opt}}^g$	$\log(\text{C}/\text{O})_{\text{UV}}^h$			
	(C III] $\lambda 1908$ )	(O III] $\lambda 1666$ )	([O II] $\lambda 3727$ )	([O III] $\lambda 5007$ )				
J084236	1.79±0.06	0.743±0.309	0.529±0.316	0.426±0.016	5.150±0.110	7.63±0.01	-0.823±0.114	-0.900±0.161
J094718	1.61±0.05	1.166±0.233	0.219±0.237	0.698±0.020	5.411±0.116	7.76±0.01	-0.556±0.079	-0.384±0.111
J095430	1.69±0.06	1.001±0.154	0.471±0.078	0.590±0.019	5.418±0.116	7.71±0.01	-0.669±0.111	-0.757±0.157
J100348	1.57±0.05	1.133±0.136	0.409±0.050	0.452±0.017	6.831±0.143	7.87±0.01	-0.587±0.129	-0.626±0.182
J113116	1.67±0.07	1.089±0.141	0.316±0.143	0.872±0.035	5.678±0.126	7.72±0.01	-0.664±0.142	-0.575±0.200
J120202	1.83±0.06	0.679±0.071	0.275±0.057	0.529±0.016	3.660±0.078	7.48±0.01	-0.780±0.093	-0.690±0.131
J121402	1.74±0.06	1.293±0.078	0.417±0.078	0.646±0.018	5.137±0.108	7.65±0.01	-0.580±0.102	-0.595±0.144
J132347	1.74±0.04	0.708±0.071	0.619±0.071	0.218±0.012	7.222±0.152	7.78±0.01	-0.873±0.079	-0.912±0.111
J132853	1.60±0.05	0.475±0.063	0.241±0.122	0.829±0.023	5.002±0.105	7.75±0.01	-0.921±0.116	-0.836±0.164
J133126	1.63±0.04	1.077±0.103	0.542±0.108	0.701±0.019	5.566±0.115	7.76±0.01	-0.616±0.075	-0.807±0.106
J141851	1.86±0.05	1.247±0.068	0.713±0.069	0.410±0.013	4.634±0.095	7.56±0.01	-0.600±0.065	-0.800±0.092
J150934	1.61±0.04	0.932±0.093	0.505±0.110	0.483±0.014	6.869±0.143	7.84±0.01	-0.711±0.087	-0.799±0.123
J171236	1.52±0.05	1.186±0.172	0.361±0.106	0.738±0.020	5.911±0.126	7.86±0.01	-0.510±0.102	-0.609±0.144
J223831	1.80±0.06	1.090±0.185	0.494±0.184	0.307±0.014	4.902±0.094	7.60±0.01	-0.620±0.085	-0.681±0.120

<sup>a</sup>Observed flux in  $10^{-16}$  erg s $^{-1}$  cm $^{-2}$ .

<sup>b</sup>Restframe equivalent width in Å.

<sup>c</sup>Extinction coefficient for H $\beta$ , C III]  $\lambda 1908$  and O III]  $\lambda 1666$  emission lines.

<sup>d</sup>Correction factor used to adjust observed UV spectrum with the modelled SED.

<sup>e</sup> $t(\text{O III}) = T_e(\text{O III})/10^4\text{K}$ , where  $T_e(\text{O III})$  is the electron temperature in O $^{2+}$  zone derived by the direct method.

<sup>f</sup>Extinction-corrected flux ratios.

<sup>g</sup>C/O abundance ratio is derived using C III]  $\lambda 1908$  and [O III]  $\lambda 4959, 5007$  emission-line fluxes.

<sup>h</sup>C/O abundance ratio is derived using C III]  $\lambda 1908$  and O III]  $\lambda 1666$  emission-line fluxes.

**Table B3.** Characteristics for the determination of the C/O abundance ratio in galaxies from [Ravindranath et al. \(2020\)](#)

Name	$F^a$ (C III] $\lambda 1908$ )	EW <sup>b</sup> (C III] $\lambda 1908$ )	$F^a$ (O III] $\lambda 1666$ )	EW <sup>b</sup> (O III] $\lambda 1666$ )	$F^a$ (H $\beta$ $\lambda 4861$ )	EW <sup>b</sup> (H $\beta$ $\lambda 4861$ )	$C_{\text{int}}^c$ (H $\beta$ $\lambda 4861$ )	$C_{\text{int}}^c$ (C III] $\lambda 1908$ )	$C_{\text{int}}^c$ (O III] $\lambda 1666$ )	corr. <sup>d</sup>
J030321-075923	10.3±1.1	8.0±0.9	...	...	62.7±0.8	140±2	0.024±0.030	0.078±0.098	...	3.333
J081552+215623	13.0±1.6	10.4±1.3	...	...	34.3±1.1	257±8	0.060±0.033	0.144±0.079	...	1.000
J091113+183108	4.9±1.1	2.5±0.6	...	...	37.7±1.3	83±3	0.336±0.031	0.804±0.074	...	0.934
J105330+523752	6.1±2.3	1.9±0.7	...	...	51.4±1.5	92±2	0.120±0.031	0.287±0.074	...	1.333
J113303+651341	4.2±1.1	4.2±1.1	...	...	24.1±0.5	110±2	0.000	0.000	...	2.326
J113722+352426	9.7±2.5	3.3±0.8	...	...	65.8±1.6	128±3	0.124±0.030	0.297±0.072	...	1.250
J121903+152608	30.2±2.3	13.3±1.0	...	...	62.1±1.5	279±7	0.048±0.030	0.115±0.072	...	0.714
J124423+021540	8.5±1.1	8.7±1.2	...	...	126.0±2.1	197±3	0.072±0.028	0.172±0.067	...	5.000
J124834+123402	7.9±1.2	5.9±0.9	...	...	21.1±0.8	144±6	0.065±0.064	0.156±0.154	...	1.176
J145735+223201	18.3±1.2	16.3±1.1	...	...	90.0±1.8	235±5	0.160±0.029	0.383±0.069	...	2.222

Name	$t(\text{O III})^e$	(C III] $\lambda 1908$ )	$I(\lambda)/I(\text{H}\beta)^f$ (O III] $\lambda 1666$ )	([O II] $\lambda 3727$ )	([O III] $\lambda 5007$ )	12+log(O/H)	log(C/O) <sub>opt</sub> <sup>g</sup>	log(C/O) <sub>UV</sub> <sup>h</sup>
J030321-075923	1.53±0.06	0.611±0.065	...	0.986±0.031	5.816±0.127	7.86±0.01	-0.821±0.112	...
J081552+215623	1.43±0.06	0.459±0.057	...	0.701±0.029	7.118±0.160	8.00±0.01	-0.902±0.112	...
J091113+183108	1.26±0.13	0.357±0.080	...	2.006±0.063	3.519±0.086	7.99±0.03	-0.650±0.231	...
J105330+523752	1.22±0.09	0.232±0.052	...	1.973±0.056	4.570±0.104	8.10±0.02	-0.872±0.229	...
J113303+651341	1.41±0.10	0.407±0.106	...	1.460±0.054	5.751±0.141	7.96±0.02	-0.910±0.152	...
J113722+352426	1.19±0.06	0.274±0.071	...	1.784±0.049	5.025±0.112	8.16±0.02	-0.783±0.106	...
J121903+152608	1.51±0.05	0.405±0.031	...	0.628±0.022	6.417±0.140	7.89±0.01	-0.986±0.096	...
J124423+021540	1.21±0.04	0.425±0.057	...	1.476±0.038	5.845±0.125	8.17±0.01	-0.660±0.129	...
J124834+123402	1.26±0.10	0.543±0.082	...	1.606±0.094	6.888±0.287	8.12±0.08	-0.629±0.138	...
J145735+223201	1.41±0.04	0.755±0.049	...	0.970±0.028	7.333±0.154	8.04±0.01	-0.700±0.100	...

<sup>a</sup>Observed flux in  $10^{-16}$  erg  $\text{s}^{-1}$   $\text{cm}^{-2}$ .<sup>b</sup>Restframe equivalent width in Å.<sup>c</sup>Extinction coefficient for H $\beta$ , C III]  $\lambda 1908$  and O III]  $\lambda 1666$  emission lines.<sup>d</sup>Correction factor used to adjust observed UV spectrum with the modelled SED.<sup>e</sup> $t(\text{O III}) = T_e(\text{O III})/10^4\text{K}$ , where  $T_e(\text{O III})$  is the electron temperature in  $\text{O}^{2+}$  zone derived by the direct method.<sup>f</sup>Extinction-corrected flux ratios.<sup>g</sup>C/O abundance ratio is derived using C III]  $\lambda 1908$  and [O III]  $\lambda 4959, 5007$  emission-line fluxes.<sup>h</sup>C/O abundance ratio is derived using C III]  $\lambda 1908$  and O III]  $\lambda 1666$  emission-line fluxes.